Canadian Geotechnical Journal

Research Article

HPMC viscous fluid for centrifuge modelling

T.O. Quinten, A.A. Askarinejad, K. Gavin, and M.A. Cabrera

Department of Geoscience and Engineering, Delft University of Technology, Stevinweg 1, Delft 2628CN, The Netherlands

Corresponding author: **T.O. Quinten** (email: T.O.Quinten@tudelft.nl)

Abstract

Dynamic pile installation is a challenging aspect of the realization of offshore infrastructure. Due to the large-scale and specialized hardware involved, researchers have resorted to centrifuge modelling to study this process at a manageable scale and in a controlled environment. However, in centrifuge models, a discrepancy between the dynamic and diffusive timescales is introduced. By using a viscous fluid, the discrepancy is mitigated, thereby synchronizing both timescales. Hydroxypropylmethylcellulose (HPMC) is a versatile and affordable thickening agent, widely used in centrifuge modelling of dynamic processes. However, the rheological behavior of HPMC solutions can vary based on the type of HPMC and the solution concentration. This study investigates how the rheological behavior of HPMC solutions is influenced by the concentration and the type of HPMC. We present a detailed preparation protocol for preparing aqueous HPMC solutions and propose a generic power-law function that unifies experimental results from our study and those of previous works. We investigate the implications of varying degrees of shear thinning, as observed across different HPMC products, by examining the pore pressure response during the dynamic installation of a pile in dense sand saturated with fluids of similar dynamic viscosity. Our findings support the use of viscous fluids for studying dynamic events in the centrifuge but also emphasize the importance of selecting a viscous fluid whose rheology does not vary considerably within the range of expected shear rates. In broader terms, this work streamlines the manufacturing of viscous fluids for use in the centrifuge and advances research efforts related to modelling dynamic phenomena in geotechnical engineering.

Key words: physical modelling, offshore geotechnics, piles, dynamic installation, viscous fluid

Résumé

L'installation dynamique de pieux constitue un aspect difficile de la réalisation des infrastructures offshore. En raison du matériel spécialisé et à grande échelle impliqué, les chercheurs ont recouru à la modélisation par centrifugeuse pour étudier ce processus à une échelle gérable et dans un environnement contrôlé. Cependant, dans les modèles par centrifugeuse, une disparité entre les échelles de temps dynamiques et diffuses est introduite. En utilisant un fluide visqueux, la disparité est atténuée, synchronisant ainsi les deux échelles de temps. L'hydroxypropylméthylcellulose (HPMC) est un agent épaississant polyvalent et abordable, largement utilisé dans la modélisation par centrifugeuse des processus dynamiques. Cependant, le comportement rhéologique des solutions d'HPMC peut varier en fonction du type d'HPMC et de la concentration de la solution. Cette étude examine comment le comportement rhéologique des solutions d'HPMC est influencé par la concentration et le type d'HPMC. Nous présentons un protocole détaillé pour la préparation des solutions aqueuses d'HPMC et proposons une fonction de loi de puissance générique qui unifie les résultats expérimentaux de notre étude et ceux des travaux précédents. Nous examinons les implications des différents degrés de fluage par cisaillement, tels qu'observés dans les différents produits HPMC, en analysant la réponse de la pression interstitielle lors de l'installation dynamique d'un pieu dans du sable dense saturé de fluides ayant une viscosité dynamique similaire. Nos résultats soutiennent l'utilisation de fluides visqueux pour l'étude des événements dynamiques dans la centrifugeuse, tout en soulignant l'importance de sélectionner un fluide visqueux dont la rhéologie ne varie pas de manière significative dans la plage des taux de cisaillement attendus. Plus généralement, ce travail simplifie la fabrication de fluides visqueux pour une utilisation dans la centrifugeuse et fait progresser les efforts de recherche liés à la modélisation des phénomènes dynamiques en génie géotechnique.

Mots-clés : modélisation physique, géotechnique offshore, pieux, installation dynamique, fluide visqueux

1. Introduction

Centrifuge modelling proves valuable in providing the necessary insights in a controlled environment, at a manageable scale, and at a fraction of the cost of full-scale tests. Specifically, it is effective in examining processes in which pore pressures are generated under dynamic loads and their subsequent dissipation, both of which affect the behavior of the soil due to their influence on the effective soil stress. The

principle of centrifuge modelling involves reducing the dimensions of a geotechnical model by a factor N and upscaling the gravitational field by the same factor. The acceleration amplification factor N denotes the ratio of the model acceleration to Earth's gravitational acceleration, $g \approx 9.81$ m/s^2. Contrary to field conditions, the generation of excess pore pressures, a dynamic process, and the subsequent dissipation, a diffusive process, are non-synchronous for centrifuge modelling tests (Garnier et al. 2007). The discrepancy between the associated timescales should be accounted for in the design of the centrifuge test campaign. In a centrifuge model, the dynamic time is scaled down by a factor of N, while the diffusive time, for which time scale can be derived from the solution of the 1D differential equation for consolidation, scales by $1/N^2$.

This difference can be overcome in two ways. First, the soil intrinsic permeability could be downscaled by reducing the grain-size distribution in the model (Steedman and Ledbetter 1994). However, this reduction in grain size can change the mechanical behavior of the soil, leading to differences in the responses observed at the model and prototype scale. Secondly, a viscous fluid with a kinematic viscosity N times greater than the prototype fluid (e.g., water) can be used. In this approach, diffusive processes are slowed down N times, thus synchronizing the diffusive and dynamic timescales. It is important to note that scaling the kinematic viscosity solely safeguards the compatibility between the model and the prototype in terms of soil permeability and not in the soil stress state per se. To achieve stress equivalence between the model and prototype, the pore fluid density should be similar (Stewart et al. 1998). Further details on the scaling principles for centrifuge modelling, focusing on matching the time scales for diffusion, dynamic, and convection processes, are presented in Appendix A.

Various types of viscous fluid have been used by the physical modelling community; these include a mixture of glycerine and water (Bowman et al. 2010; Askarinejad et al. 2015) an aqueous solution of Hydroxypropylmethylcellulose (HPMC) (Allard and Schenkeveld 1994; Dewoolkar et al. 1999) an aqueous solution of carboxymethylcellulose (lCMC) (Terwindt et al. 2020), or mixtures of water and kaolin (Cabrera et al. 2018), among others. For studies in which stress equivalence between the model and prototype is important, it has been proven more practical to incorporate a cellulose-based viscous fluid into the centrifuge model, as it has a density of roughly 1000 kg/m^3.

Several groups have proposed methodologies for the preparation of aqueous methylcellulose (MC) solutions for centrifuge modelling using Methocel F50 (Stewart et al. 1998; Adamidis and Madabhushi 2015) or Methocel F450 (Gao and Vulpe 2022), both manufactured by DuPont. For preparing solutions based on lCMC, a preparation methodology is presented by Terwindt et al. (2020). However, among these studies, the relationships that relate the concentration of the solution to the obtained viscosity differ considerably.

It is hypothesized that the most influential contribution to the reported behavioral deficiencies, stems from manufacturing tolerances on the composition of the HPMC-based thickening agents. An example of the latter can be found in the study conducted by Adamidis and Madabhushi (2015) on Methocel F50, when comparing their results against those obtained by Stewart et al. (1998), a significant difference was reported in the viscosity as a function of the concentration. This observation is unexpected as both studies used the same thickening agent, Methocel F50, and adhered to a standardized preparation protocol, while using equivalent equipment. This raises concerns about repeatability between laboratories and points towards room for improvements within the current preparation protocol. Limited disclosure of details on the preparation process and the equipment used are a minor factor contributing to this discrepancy.

This work aims to present an explicit standardized protocol for the preparation of aquaous solutions of various types of HPMC and evaluate their performance in a dynamic centrifuge model. This study focuses on three grades of HPMC, namely: (i) F50; (ii) F450; (iii) F4M, where the nominal viscosity of an aqueous solution at 2% mass concentration is 50, 450, and 4000 mPa·s, respectively. The solution's rheological properties are characterized over shear rates ranging from 0.1 to 1000 s^{-1} (Section 2.3). The results show a reduction in the linear viscoelastic region (LVR) and increased shear-thinning behavior with higher nominal viscosity and concentration (Section 4.1). A power-law fit adequately captures the relationship between viscosity and concentration for each HPMC solution, although the fitted coefficients differ from those reported in previous studies. To account for variations in the chemical composition of HPMC, a modified power-law model is proposed. This relationship is calibrated to a reference viscosity at a concentration specific to each HPMC type. The aforementioned relationship largely unifies the fitting expressions proposed by previous works (Section 4.2). Finally, we use the reference case of pile driving and evaluate the influence of shear thinning on the installation response (Section 4.3). This work underlines the importance of accounting for shear rate effects in selecting the HPMC type, thereby improving model and prototype equivalence.

2. Methodology

2.1. HPMC selection

HPMC is a cellulose ether, fabricated by treating purified cellulose with methyl chloride and propylene oxide to incorporate hydroxypropyl and methyl groups into the cellulose backbone. The resulting compound is subsequently purified and ground to a fine white powder. HPMC is a non-toxic, water-soluble polymer that presents no biological hazard to the environment. The compound is used in a wide range of industries, including but not limited to pharmaceuticals, cosmetics, coatings, and food (Sadasivuni et al. 2017). The addition of propylene oxide during the manufacturing process leads to the hydroxypropyl substitution on the anhydroglucose groups. The latter raises the hydration temperature, the temperature at which the viscosity of the solution starts to develop, to about 60 °C (The Dow Chemical Company 2002). Therefore, during the preparation of HPMC solutions, it is not required to actively cool the solution, which simplifies the preparation process. It is for this reason that the use of HPMC

Fig. 1. Hot-cold preparation method of hydroxypropylmethylcellulose (HPMC) viscous fluid. Note that the fluid needs to be de-aired before using it in a centrifuge soil model.

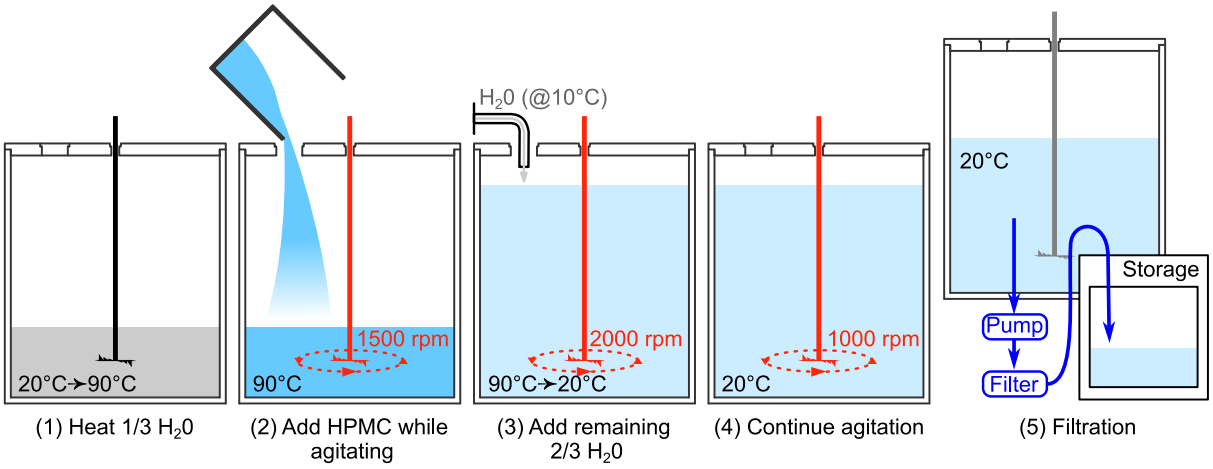

is preferred over MC, which has a hydration temperature of ≈20 °C.

The ratio of hydroxypropyl and methyl substitution on the anhydroglucose molecules governs organic solubility. For ideal water solubility, a methoxyl degree of substitution between 1.64 and 1.92 is required (The Dow Chemical Company 2002). This requirement, together with the need for hydration temperature well above ambient laboratory conditions, leads to the selection of Methocel F50, F450, and F4M as the HPMC products of interest for this study. By approximation, the nominal viscosity values at 2% mass-concentration of these three products are separated by one order of magnitude, respectively equating to viscosities of 50, 450, and 4000 mPa·s.

HPMC is available in an untreated and surface-treated variety. The surface-treated variety is temporally insoluble in cold water, which enables dispersion at temperatures below the hydration temperature. At concentrations lower than 5% by mass, the hydration temperature is a function of the solution's pH value. In order to initiate hydration of surface-treated HPMC, a base should be added to the solution. The solution viscosity will subsequently develop, under continuous agitation. For untreated powder, the fabrication process leverages the insolubility of the HPMC at high temperatures. This allows the powder to be evenly dispersed in the solvent, before the initiation of the hydration process through the addition of cooler water. The accompanying manufacturing technique is called the "hot-cold method" (The Dow Chemical Company 2002). The relatively uncomplicated preparation method of untreated HPMC and its previous use in other studies underlie the decision to use untreated HPMC.

2.2. Viscous fluid preparation

In this work, the viscous solutions are fabricated using the hot-cold method, which relies on the insolubility of HPMC at high temperatures. A schematic overview of the hot-cold preparation methodology is shown in Fig. 1. Additionally, an annotated picture of the preparation set-up is provided in Fig. 2. A detailed explanation of the preparation process is presented below.[1]

Fig. 2. Annotated overview of the preparation set-up for hydroxypropylmethylcellulose (HPMC) viscous fluids at Delft University of Technology (DUT).

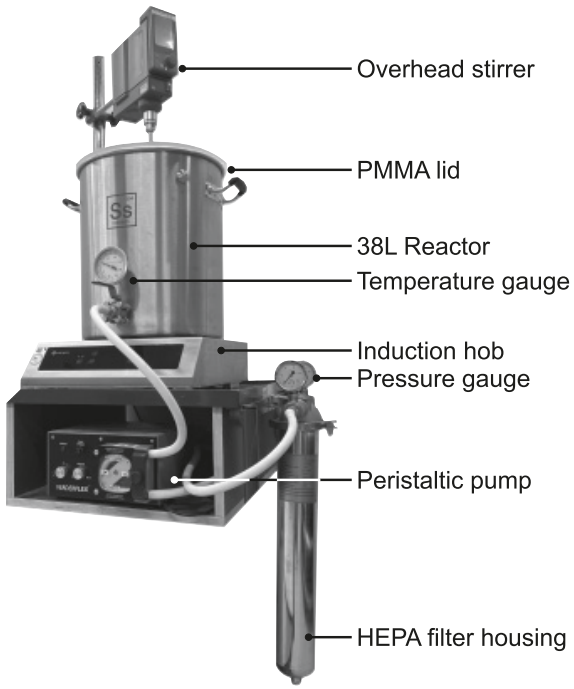

(1) Heat 1/3 of the water weight to 90 °C (step 1 in Fig. 1). The water is contained in a stainless steel reactor fitted with an analogue temperature gauge and ball valve (see Fig. 2). The reactor has a diameter of 35 cm, a height of 42 cm, and a filling capacity of 38 L. A 3.5 kW temperature-

[1] It was found that preparation is easier when all quantities are expressed by weight rather than by volume, as fluid density varies with temperature.

controlled induction hob (shown in Fig. 2) is used to heat the reactor and its contents to 90 °C. The reactor is closed with an polymethyl methacrylate (PMMA) lid, as shown in Fig. 2, which limits water evaporation. The lid is equipped with four openings: (i) a centralized opening for the mixer and alignment bearing; (ii) a cut-out to allow placement and removal of the lid when the mixer is in place; (iii) a cut-out for a digital temperature probe; and (iv) a supply opening for cold water and HPMC powder.

(2) Once the fluid has reached the desired temperature, HPMC is slowly added through the supply opening in the PMMA lid (step 2 in Fig. 1). The mixture is agitated using an IKA Eurostar 60 overhead stirrer (see Fig. 2) fitted with an 80 mm diameter IKA dispersion mixer. The stirring speed is adjusted to ensure full agitation of the solution and to prevent HPMC from remaining on the surface. In this study, complete dispersion was achieved at 1500 rpm. For practicality, HPMC is used at its natural moisture content. While the formulation could alternatively be based on the dry mass of HPMC, we account directly for the total water content (including the moisture present in the HPMC powder itself) to achieve the desired solution concentration. This approach requires that the moisture content of the powder be explicitly considered when calculating the required HPMC mass. To this end, the gravimetric water content of the HPMC, denoted as θ^*, is determined prior to preparing the viscous fluid. θ^* is defined as the ratio of the water mass in the HPMC, $W_{w,HPMC}$, to the total mass of the HPMC (wet), W_{HPMC}, as shown in eq. 1:

$$\theta^* = \frac{W_{w,HPMC}}{W_{HPMC}} \quad (1)$$

Provided that θ^* is known, the total required mass of HPMC, W_{HPMC}, can be computed from the desired concentration C (expressed as a mass fraction) and the added water mass W_w, using eq. 2:

$$W_{HPMC} = \frac{C\, W_w}{1 - \theta^* (1 + C)} \quad (2)$$

This formulation enables researchers to achieve the correct solution concentration using the as-received (moist) powder in combination with a known quantity of water. Note that θ^* must be expressed as a fraction (e.g., 0.02 for 2%) when using eq. 2.

(3) Once the HPMC is fully dispersed, the induction hob is switched off while agitation continues. Cold water is added to the solution through the supply opening (step 3 in Fig. 1). Due to the increase in fluid volume, it is advisable to gradually increase the stirring revolutions, maintaining the solution in full agitation. For this study, this meant operating the stirrer up to a maximum of 2000 rpm. Following the addition of cold water, the maximum agitation is maintained for 5 min. Subsequently, the stirring is reduced to 1000 rpm and the fluid is left to cool to room temperature (step 4 in Fig. 1). Fluid temperature is monitored through a digital temperature probe that is connected to the overhead stirrer. The solution temperature can also be determined from an analogue temperature gauge on the front of the reactor (see Fig. 2).

(4) Once the fluid has reached room temperature, the stirrer is switched off. Subsequently, the ball valve on the reactor is connected to the filtration set-up by means of a peristaltic hose that is fed through a peristaltic pump (see Fig. 2). When the pump is engaged and the valve is open, fluid is forced through a 5 μm glass-fiber high-efficiency particulate air (HEPA) filter, before exiting through an outlet, where it is collected in a storage vessel (step 5 in Fig. 1). The filtration set-up has two pressure gauges to monitor the hydraulic head loss over the filter, as shown in Fig. 2. The head difference is a function of the filter permeability and the flow rate imposed by the peristaltic pump. Repeated use of the filter can lead to particle accumulation, which increases the flow resistance and is indicative of the opertional condition of the HEPA filter. For this reason, the pressure drop is monitored during operation to ensure timely replacement of the filter and safeguard the filtration efficiency. For this study, the replacement threshold is set at a head difference that exceeds 2 bar. Due to the high purity of the HPMC, the operational lifetime of the HEPA filter exceeded 1000 L of solution.

(5) Following the filtration process, the fluid is de-aired. This removes dissolved air from the solution, which could be problematic during sample saturation. The filtered and de-aired fluid is stored in a climate-controlled room at 20 °C until use. The work of Adamidis and Madabhushi (2015) demonstrated that aging does not significantly influence the fluid's properties in the 30 days following preparation. This finding is confirmed by conducting periodic viscosity measurements from the same batch of viscous fluid, which showed negligible viscosity fluctuations ($\leq$1 mPa·s) over a period of 10 months. During this time, the fluid was stored in a sealed and light-tight container inside a 5 °C cold room at a relative humidity of 80%.

2.3. Rheological measurements

The rheology of the HPMC solutions is determined using an Anton Paar MCR302 rheometer, which shears the sample between a stationary outer cylinder and a rotating measuring spindle. Due to the precise measurement of the rotational torque and the know dimensions of the measuring spindle, the shear stress, τ, can be computed. It is possible to estimate the fluid dynamic viscosity, μ, by assuming an isotropic and incompressible fluid, where the shear stress, τ, is related to the acting shear rate, $\dot{\gamma}$, as $\tau = \mu\dot{\gamma}$.

Each experiment requires approximately 15 mL of fluid, which is placed inside the measuring cup using a syringe. Care was taken to avoid air entrainment as it alters the rheological measurements (Struble and Jiang 2004). The rheological measurements are performed at a fluid temperature of 20 ± 0.1 °C, which is controlled using an integrated electrical temperature device.

For each experiment, four consecutive logarithmic strain sweeps are conducted across a shear rate range of $\dot{\gamma} \in [0.1 : 1000]$ s^{-1}. For each decade in this range, 10 measure-

Fig. 3. Normalized flow curves of aqueous solutions of F50, F450, and F4M at roughly 50 mPa·s viscosity. Non-dimensionalized flow curves (inset plot) were non-dimensionalized by μ^*, the viscosity obtained at $\dot{\gamma}^* = 10\ s^{-1}$, as indicated by the vertical dashed line. Labels indicate the solution concentration in percent.

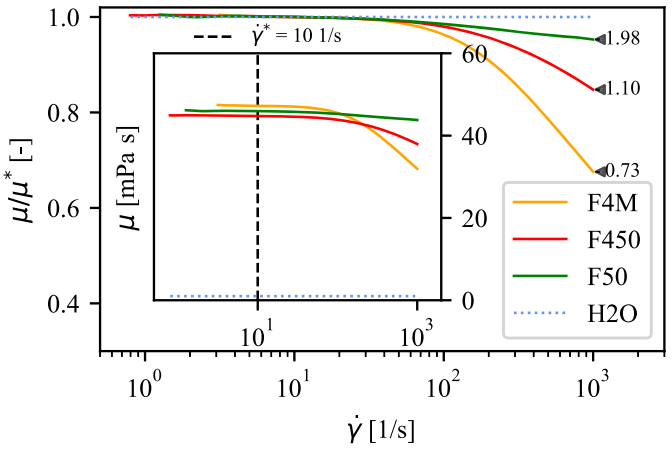

ments are taken, totalling 164 measurements per test. The measurement duration is calculated using an inverse logarithmic relationship with the shear rate, $\dot{\gamma}$. The measurement duration bounds are set to 15 s for the lowest $\dot{\gamma} = 0.1\ s^{-1}$ and 1 s for the highest $\dot{\gamma} = 1000\ s^{-1}$. For intermediate shear rates, the rheometer automatically adjusts the measurement time following the inverse logarithmic relationship. This approach makes it possible to optimize the test duration without compromising the measurements' reliability (Anton Paar 2024).

From the strain sweep analysis, a flow curve is obtained, which illustrates the variation of the solution's viscosity with respect to shear rate, as demonstrated in Fig. 3. The inset plot of Fig. 3 shows the flow curves for aqueous solutions of Methocel F50, F450, and F4M. For all solutions, the LVR viscosity, μ^*, is approximately 50 mPa·s. The LVR viscosity is the viscosity measured at the normalizing shear rate, $\dot{\gamma}^*$, within the shear rate range where viscosity remains constant. In Fig. 3, $\dot{\gamma}^* = 10\ s^{-1}$ for all fluids, as indicated by the vertical dashed line. For reference, the result of a strain sweep analysis on water is also included in Fig. 3 and is shown as the horizontal dotted line. The outer plot of Fig. 3 shows the result of normalization of flow curves by μ^*. Water, unlike the viscous fluids, exhibits shear-rate-independent viscosity. The flow curve is therefore horizontal, which is characteristic of Newtonian flow behavior. Curving flow curves indicate non-Newtonian flow behavior, a feature that is present to varying degrees for the viscous fluids subject of this study.

While temperature effects on viscosity were not explicitly measured in this study, the work of Adamidis and Madabhushi (2015) and Gao and Vulpe (2022) demonstrate that HPMC solutions experience changes in their effective viscosity by changing the fluid temperature (explored between 10 and 25 °C), regardless of whether Methocel F50 or F450 is used. It is therefore expected that F4M solutions behave similarly, provided their viscosity falls within the range explored in the aforementioned studies. All samples in this study were stored in a climate-controlled room at 20 °C prior to testing. Due to the dynamic nature of the experiments, each test lasted less than 1 h. Given the short duration and the large size of the specimens (approximately 30 kg), slight temperature fluctuations within the centrifuge facility are unlikely to have appreciable effects on the fluid temperature. Consequently, temperature-induced variation in viscosity is not expected to have influenced the results. As a general guideline, the authors recommend that the need to account for temperature effects is evaluated based on the characteristics of the test facility, the duration of testing, and the size of the sample.

3. Centrifuge tests

The reduction of viscosity with shear rate, as observed for aqueous solutions of F50, F450, and F4M in Fig. 3, is known as shear thinning (Mezger 2016). Shear thinning is a common feature of the rheology of polymer solutions, as the molecules tend to untangle due to the imposed shear. Because the viscosity of these fluids varies with shear rate, a similar change in the soil's drainage properties is expected. It is important to evaluate the impact of such a change on the saturated soil response for dynamic centrifuge tests in saturated samples, that rely on these viscous fluids. Given that the observed viscosity reduction is nonlinear and most pronounced at higher shear levels, this is particularly relevant for pile installation tests, as they involve intense, localized shear over short time intervals. Therefore, three dynamic pile installation tests were conducted in the geotechnical centrifuge facility at Delft University of Technology (DUT) to evaluate the influence of pore fluid rheology on the observed behavior. Between tests, the soil saturation medium varies and consists of either water (H_2O), an aqueous solution of Methocel F50 or Methocel F4M. For F50 and F4M, the LVR viscosities are 45.3 and 48.3 mPa·s, recorded at shear rates of 10 and 5.01 s^{-1}, respectively. All tests are conducted at 50 *g*. The 50 *g* radius coincides with 1/3 of the sample height, as measured from the soil surface. The model pile dimensions are as follows: outer diameter, $D_P = 42$ mm; wall thickness, $t_P = 2$ mm; and, length, $L_P = 175$ mm. The sample consists of GEBA sand, prepared at 80% relative density. Table 1 provides an overview of the soil properties of GEBA sand.

The strongbox consists of the cylindrical PVC container of 295 innner diameter and 180 mm internal height. The strongbox is instrumented with nine pore pressure transducers (PPTs), tracking the saturated soil response during installation at three different depths (i.e., $z = [1D_P; 2D_P; 3D_P]$) and three radial distances from the pile wall (i.e., $r = [1D_P; 1.5D_P; 2D_P]$). The PPTs consist of a MPXH6400A absolute pressure transducer, with a measurement range between 20:400 kPa and a response time of 1 ms, connected to a stainless steel tube that extends through the side wall of the strongbox. The tube has an outer diameter of 3.2 mm and a wall thickness of 1 mm. Within the strongbox, the inner end of the tube is fitted with a Bentheimer sandstone filter of 6.6 mm diameter, and with an air-entry value of 20 kPa. This configuration allows pore pressure transmission from the soil to the sensing

Table 1. GEBA sand material properties (Maghsoudloo et al. 2018; Maghsoodi et al. 2022; Kementzetzidis et al. 2023).

Property	Symbol	Value	Unit	Standard
Median particle size	D_{50}	0.11	mm	
Curvature coefficient	C_c	1.24	–	
Uniformity coefficient	C_u	1.59	–	
Specific gravity	G_s	2.67	–	
Minimum void ratio	e_{min}	0.64	–	JIS A 1224:2009
Maximum void ratio	e_{max}	1.07	–	JIS A 1224:2009
Minimum dry density	ρ_{min}	12.63	kN/m^3	
Maximum dry density	ρ_{max}	15.94	kN/m^3	
Critical friction angle	φ_c	31.7	°	ISO 17892-9:2018

Fig. 4. Instrumented strongbox, equipped with nine pore pressure transducers (PPTs) positioned at fixed depths and radial distances relative to the model centroid. The base of the strongbox contains a removable 15 mm thick insert fitted with four Bentheimer sandstone filter plates to facilitate uniform sample saturation while flushing fluid through the inlet at the base of the strongbox.

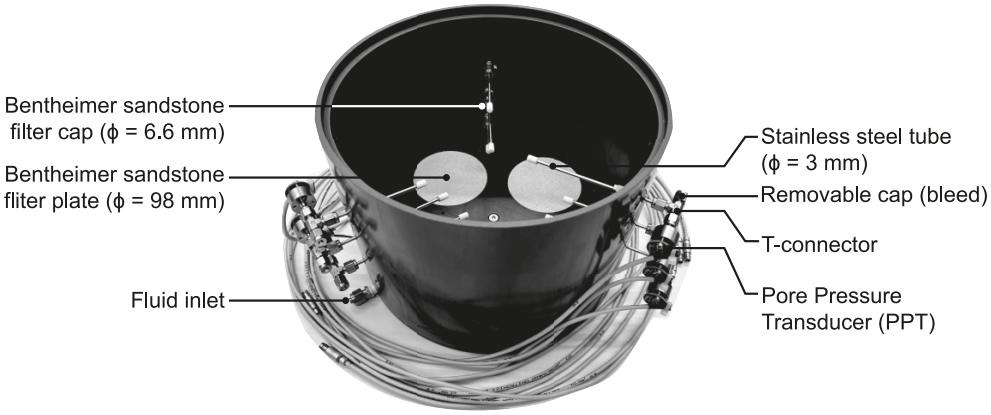

unit while preventing the tube from clogging. Externally, the tube connects to a T-connector. One end of the T-connector is coupled to the pressure sensor, while the other end is fitted with a removable cap, which can also be used to bleed the sensor. Figure 4 shows an annotated image of the strongbox and its relevant components.

During sample preparation, the cap on the T-connector is removed and fitted with a hose that is connected to a syringe. By pulling the syringe's plunger outward, suction is applied to the system, which forces fluid from the sample through the tubing. This process removes any air trapped within the tubes that could affect the pressure readings during testing. The latter ensures full saturation of the sensor before testing. The tube itself is designed to remain rigid under dynamic loading conditions, thereby securing the porous stone's position within the soil sample and preventing displacement during testing. This configuration assumes that the advantages of incorporating fixed measuring points within the soil model outweigh the localized increase in stiffness and the resulting stress concentrations along the instrumentation tube.

The pile installation procedure consists of two phases: (i) the self-weight pile penetration phase, and (ii) the dynamic pile installation phase. The self-weight pile penetration phase is divided into two and occurs first at 1g, and subsequently at *Ng*. At 1g, the ram is placed on the anvil and the ensemble consisting of the pile, anvil, and ram is positioned at the soil surface. Subsequently, the ensemble is released and allowed to settle freely by self-weight. When the pile embedment stabilizes, the centrifuge is accelerated to 50 *g*. This marks the start of the second self-weight penetration stage. Once the settlement has stabilized, the centrifuge is brought to a standstill to manually configure the actuator for the first blow of the pile driving sequence. The initial pile installation configuration, where the ram mass is suspended above the pile, is shown in Fig. 5. The combined self-weight settlement is denoted as L_{inital}/D_P and is provided for each experiment in Table 2. Table 2 illustrates that self-weight penetration settlement is similar between all tests. Indicating soil conditions are consistent between the tests.

Following the self-weight penetration phase, the model pile is dynamically installed using a series of blows using the prolonged blow simulator of DUT (Quinten et al. 2022). The actuator specifications are outlined hereafter, please observe that all parameters are in model scale, with the prototype equivalent listed between parentheses. The actuator is fitted with a 1.899 kg (236 t) ram mass and the stroke is set to 40 mm (2 m). On average, the kinetic energy of the ram is equivalent to 27.4 J (3.43 MJ) upon impact, at a velocity of 5.4 m/s

Fig. 5. Photograph of the prolonged blow simulator of Delft University of Technology (DUT) in the centrifuge basket, in its initial pile installation configuration (ram mass suspended by the electromagmnet above the pile).

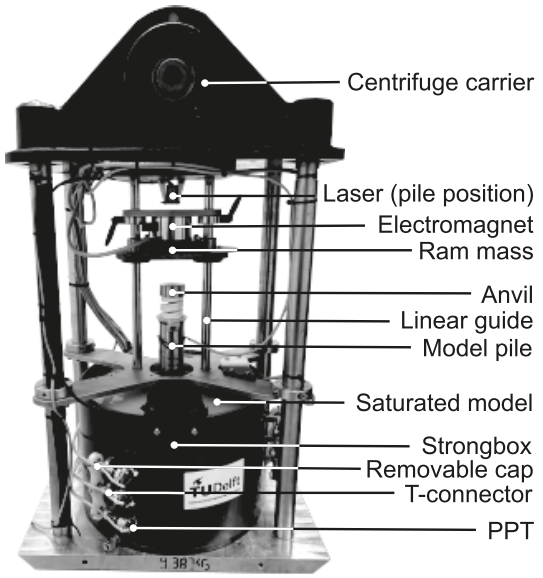

Table 2. Summary of pile installation tests for different fluids; [(1)]measured at $\dot{\gamma} = 5.01$ s^{-1}; [(2)]measured at $\dot{\gamma} = 10$ s^{-1}.

Fluid	D_r [%]	μ [mPa·s]	$L_{initial}/D_P$ [-]	L_{final}/D_P [-]
Water	82	1	1.47	3.06
F4M	81	48.3[(1)]	1.54	2.81
F50	85	45.3[(2)]	1.62	2.80

Note: The subscripts initial and final refer to the self-weight penetration prior to the first blow and the embedment depth after completion of the test, respectively.

(5.4 m/s). These parameters are idealized and do not account for energy losses during the guided translation of the ram from its initial position to the anvil on top of the model pile. The increase in impact energy due to the rising average acceleration over the fixed falling height (40 mm), resulting from the settlement of the pile during the test, is also unaccounted for.

As the actuator lacks the functionality to raise the ram mass in flight, the centrifuge is halted and restarted between blows to manually reset the falling height of the hammer. Each pause lasts approximately 5 min, excluding the time required to stop and restart the centrifuge. Intermittent halting of the centrifuge means that the post-blow stress state is not preserved between blows, leading to soil relaxation and excess pore pressure dissipation. Upon centrifuge re-initiation, only the global stress state is recovered. As all tests are affected by this shortcoming, conclusions following from comparative analysis of the results remain valid Tests are terminated once the pile embedment depth reaches $\approx 3 \sim D_P$. Table 2 provides the final pile embedment depth, L_{final}/D_P, at termination for all three tests.

4. Results

This section presents the results from the rheological characterization of the HPMC-based viscous fluid and the centrifuge study on the influence of shear thinning on dynamic pile installation. We introduce a unified framework for determining the HPMC's concentration to obtain the desired viscosity. Additionally, we demonstrate the influence of shear thinning on the experimental observations from the centrifuge test campaign.

4.1. Viscosity as a function of shear rate

As mentioned in Section 2.3, the relationship between viscosity and shear rate can be captured inside a flow curve. For water, a Newtonian fluid, the viscosity is independent of the shear rate. Aqueous solutions of HPMC however are non-Newtonian as their viscosity decreases at higher shear rates. This results in a decrease of the solution's viscosity as the shear rate increases and is evident from the flow curves shown in the inset plots of Figs. 6*a*, 6*b*, and 6*c*.

To better capture the degree of shear thinning between aqueous solutions of different types of HPMC, the flow curves are normalized by μ^*, obtained at $\dot{\gamma}^* = 10$, 10, and 5.01 s^{-1} for F50, F450, and F4M, respectively. A lower $\dot{\gamma}^*$ is used for F4M because the LVR does not extend to 10 s^{-1} for the whole range of solution concentrations. The resulting curves are displayed in the outer plots of Figs. 6*a*, 6*b*, and 6*c*. The labels next to the arrowheads show the solution's concentration, C, in percent. From Fig. 6, it is evident that all aqueous solutions of HPMC exhibit a non-Newtonian behavior, demonstrating progressive shear-thinning with increasing shear rate (for a constant C).

For solutions with an LVR viscosity of approximately 50 mPa·s, the relative decrease in apparent viscosity at the maximum shear rate of 1000 s^{-1} is 5%, 15%, and 40% for F50, F450, and F4M, respectively. This observation aligns with the findings of McMullen et al. (2022), who hypothesized that the shear-thinning behavior of aqueous HPMC solutions correlates with the polymer's molecular mass or chain length. Using the HPMC manufacturer's terminology, this implies that within the shear rate range considered in this study, the extent of shear thinning correlates with the HPMC viscosity grade. Moreover, it is observed that the shear rate at which shear thinning effects are first observed decreases with the viscosity grade. The span of the LVR therefore reduces. Both observations also hold when looking at the effect of solution concentration on the flow curves for each type of HPMC individually. The relative viscosity reduction at the maximum shear rate increases with the concentration for all HPMC grades. In addition, for the same HPMC type, an increase in concentration progressively shortens the LVR span. These observations demonstrate that HPMC grade and solution viscosity both affect shear thinning.

In the context of experimental modelling, it is recommended to consider these effects during the selection of the HPMC type, so fluid properties remain reasonably constant throughout the experiment. This is especially relevant for applications where high shear rates are anticipated. For low shear rate applications like the quasi-static loading of piles,

Fig. 6. Flow curves normalized by μ^*, the viscosity obtained at a shear rate of 10 s^{-1} for F50 and F450 and 5.01 s^{-1} for F4M (dashed vertical lines), versus shear rate, $\dot{\gamma}$. Labels indicate the solution concentration in percent. Insert plots depict the non-dimensionalized flow curves.

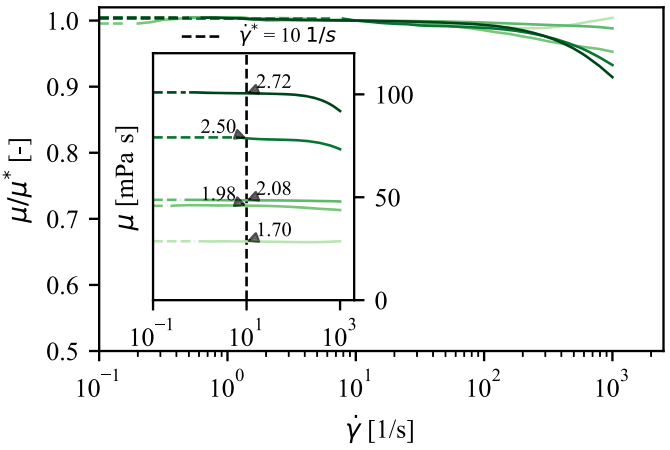

(a) Methocel F50

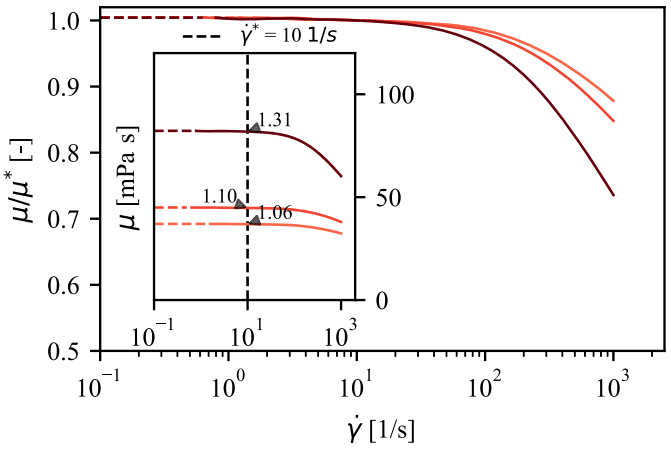

(b) Methocel F450

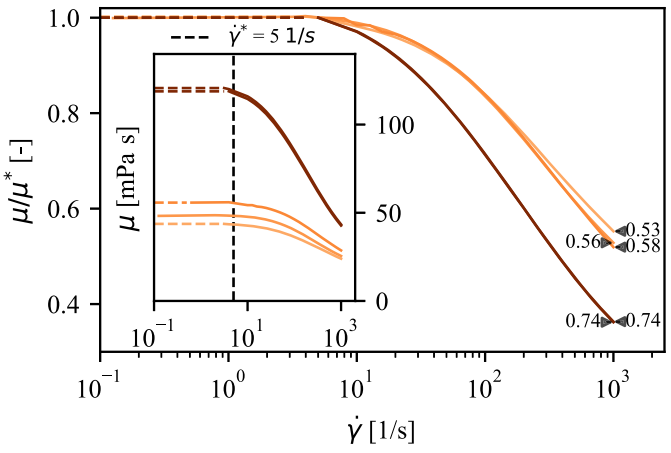

(c) Methocel F4M

caisson installation or the stability of retaining structures, among others, higher HPMC viscosity grades can arguably be used. Due to the lower concentrations required to obtain the desired viscosity, using high viscosity grades is more economical. Additionally, the unit weight of these fluids is closer to that of water, thereby providing marginally better stress compatibility between model and prototype.

4.2. Viscosity as a function of concentration

From a practical standpoint, the preparation of aqueous solutions of HPMC is informed by the relationship between the mass concentration and the solution viscosity. This underlines the need for a reliable viscous fluid production process that yields fluid with the desired viscosity in sufficient volume for the entire centrifuge modelling campaign.

The relationship between mass concentration and viscosity of F50, F450, and F4M is shown in Fig. 7. The data depicted are the average viscosity measurement, after four consecutive shear strain sweeps. All measurements were taken at 20 °C and within the LVR of each HPMC type. As such, the forthcoming relationships between concentration and viscosity purposefully omit shear thinning effects at higher shear rates. As is observed from Fig. 7, the solution viscosity increases nonlinearly with concentration and can be approximated by a power law in the form of $\mu = a \sim C^b$, where a and b are fitting constants obtained through least-squares regression, C is the solution concentration, and μ is the corresponding viscosity. The resulting fitting curves are plotted in Fig. 7 alongside power fitting relationships proposed by previous works, if available. Table 3 lists the fitting and determination coefficients of all plotted curves, please note that not all expressions use the same units for concentration and viscosity.

From Fig. 7, it can be observed that the proposed power laws adequately capture the trend in the experimental data. The determination coefficients, as listed in Table 3, further support this and are consistent with those reported in the reference studies by Adamidis and Madabhushi (2015) and Gao and Vulpe (2022), who both fitted their experimental data with similar power laws. The manufacturer of the HPMC used in this study recommends the use of an eight-order polynomial to describe the relationship between viscosity and concentration for their full product range (The Dow Chemical Company 2002). However, as noted in the work of Adamidis and Madabhushi (2015), this suggestion does not yield an optimal fit with the experimental data of their study. Consequently, Adamidis and Madabhushi (2015) proposed an adapted version, tailored to their experimental data, that produced satisfactory results but could not be unified with the results of other researchers. Tailored fitting relationships therefore remain the generally preferred solution for scientific purposes, though their applicability is intrinsically limited to one particular use case. Except for Methocel F4M, for which no reference study was found in the literature, the commonality between the fitting relationship as suggested in this study and those of previous works is limited. For Methocel F50, the findings of this study roughly fall in the range delimited by Stewart et al. (1998) and Adamidis and Madabhushi (2015). For Methocel F450, the associated fitting rela-

Fig. 7. Power-law approximations of viscosity as a function of concentration for F50, F450, and F4M, relative to (power law) fitting expressions proposed by fellow researchers. The complete overview of fitting parameters is provided in Table 3.

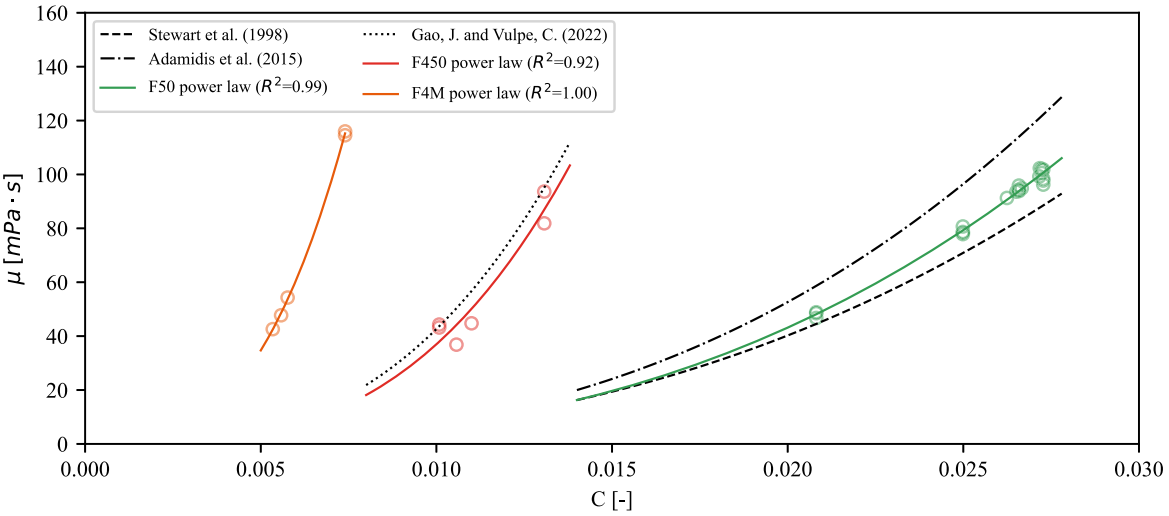

Table 3. Fitting parameters and determination coefficients for power-law approximations of the experimental data of this study and those of fellow researchers.

	Least-squares power fit: $\mu = a \cdot C^b$					
Study	Unit of C	Unit of μ	HPMC type	a	b	R^2
Stewart et al. (1998)	%	mPa·s	F50	6.92	2.54	–
Adamidis and Madabhushi (2015)	%	mPa·s	F50	8.017	2.715	0.99
This work	–	mPa·s	F50	1876 182.50	2.73	0.99
Gao and Vulpe (2022)	%	Pa·s	F450	0.0426	2.9973	0.98
This work	–	mPa·s	F450	89 154 235.85	3.19	0.92
This work	–	mPa·s	F4M	385 326 930.62	3.06	1.00

tionship consistently underpredicts the anticipated viscosities reported by Gao and Vulpe (2022); although the product type and preparation methodology were identical in both instances. When considering the concentrations required to produce viscous fluids up to a viscosity of 100 mPa·s, the mutual differences between individual fitting expressions are ≥5%.

Literature does not provide a conclusive cause for the observed divergence between fitting expressions proposed by different researchers. One possible cause is the use of bacterial inhibition agents, such as benzoic acid, as in Stewart et al. (1998). Such addition was neither used in the work of Adamidis and Madabhushi (2015) and Gao and Vulpe (2022), nor this study. However, the aforementioned studies still show a significant degree of variability in terms of fitting expressions. Furthermmore, aqueous HPMC solutions are chemically stable over a pH range of 2.0–13.0 (The Dow Chemical Company 2002). This further supports the idea that the addition of benzoic acid is not a root cause of the observed divergence.

A more plausible explanation stems from variability in product characteristics due to manufacturing tolerances. Challenges in controlling the polymeric chain length of HPMC during manufacturing result in production tolerances of up to ±10% on the reference viscosity, μ_{ref}, which is defined as the viscosity measured at a 2% mass concentration. Variations in the average polymeric chain length or molecular mass affect the viscosity across the full range of solution concentrations (McMullen et al. 2022). In practice, this uncertainty necessitates recalibrating fitting expressions whenever a new batch of HPMC is used. This is a rather unsatisfactory situation, as the recalibration process is time-consuming and requires extensive rheological characterization over a wide range of concentrations.

To address this, it is preferable to account for this variability directly in the definition of the fitting expressions. Therefore, an alternative methodology is proposed that incorporates the viscosity at a known concentration as an indirect measure of molecular mass, yielding a high-quality fitting expression without the need for extensive rheological testing. For this, let us assume that the relationship between the normalized viscosity, μ/μ_{ref}, and concentration can be expressed by a power law:

$$\frac{\mu}{\mu_{ref}} = d \cdot C^e \quad (3)$$

where C is the solution concentration, expressed as a fraction, μ_{ref} is the viscosity at a known mass-concentration C_{ref},

Table 4. Fitting parameters and determination coefficients of the generic fit applied to the data of this study and those of fellow researchers.

	Least-squares generic fit: $\mu = u_{ref} \cdot d \cdot C^{-\log_{C_{ref}}(d)}$					
Study	Unit of C	Unit of μ	C_{ref} [–]	u_{ref} [mPa·s]	d	R^2
Stewart et al. (1998)	–	mPa·s	0.02	40.25†	32 538.84	0.92
Adamidis and Madabhushi (2015)	–	mPa·s	0.02	52.64†	32 538.84	0.98
This work	–	mPa·s	0.02	44.2	32 538.84	0.99
Gao and Vulpe (2022)	–	mPa·s	0.011	56.72†	1318 668.63	0.94
This work	–	mPa·s	0.011	50.13	1318 668.63	0.92
This work	–	mPa·s	0.006	60.63	2723 039.44	0.99

†Back-calculated values.

Fig. 8. Viscosity as a function of concentration for F50, F450, and F4M, as obtained through the use of eq. 6. Associated fitting parameters are listed in Table 4.

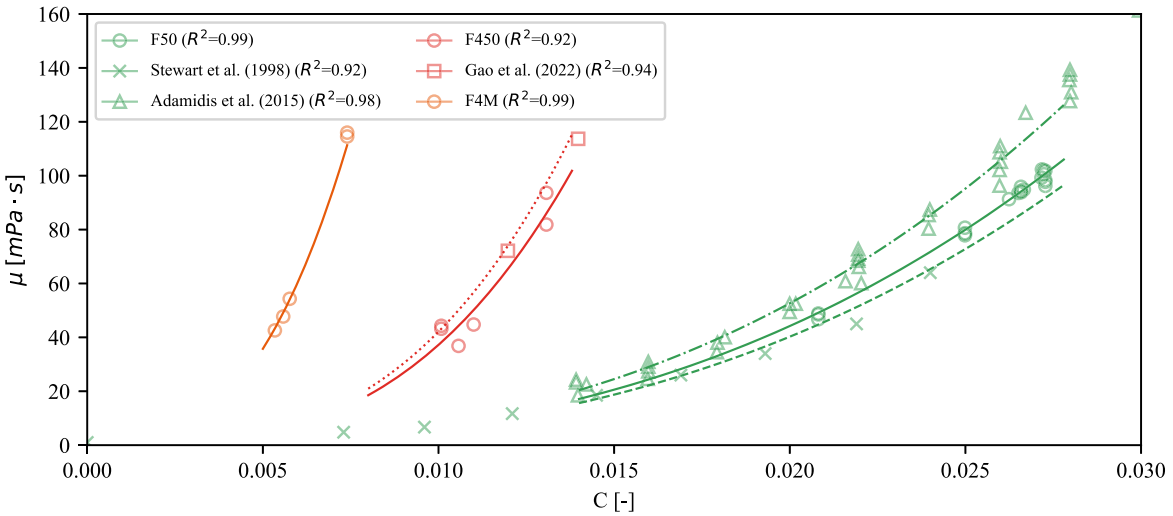

and d and e are fitting coefficients. For F50, F450, and F4M respectively, the reference concentrations are set to 0.02, 0.011, and 0.006, which respectively lie in the middle of the concentration ranges explored in this study. As μ/μ_{ref} equals unity when C_{ref} is substituted into eq. 3, the exponent e can be expressed in terms of the fitting constant d as follows:

$$e = -\log_{C_{ref}}(d) \quad (4)$$

Combining eqs. 4 and 3, yields:

$$\frac{\mu}{\mu_{ref}} = d \cdot C^{-\log_{C_{ref}}(d)} \quad (5)$$

The experimental data of this study are subsequently fitted with eq. 5 to determine the fitting constant d, which is a unique fitting parameter for each HPMC type. The resulting coefficients are included in Table 4. Finally, to obtain an expression for the absolute viscosity, both sides of eq. 5 are multiplied by u_{ref}:

$$\mu = \mu_{ref} \cdot d \cdot C^{-\log_{C_{ref}}(d)} \quad (6)$$

leaving μ_{ref} as the sole parameter required for calibrating the fitting expression. For Methocel F50, as $C_{ref} = 0.02$, μ_{ref} is generally provided in the certificate of analysis as supplied by the manufacturer. In this case, eq. 6 can be used directly to derive a fitting expression. For Methocel F450 and F4M, μ_{ref} should be determined by drafting a single test volume of fluid at C_{ref} as listed in Table 4. The latter yields sufficient information to calibrate eq. 6.

From Fig. 8, it can be observed that eq. 6 adequately captures the evolution of viscosity with concentration for both the experimental data presented in this work, and those of the reference studies. For the reference studies, μ_{ref} was computed by evaluating the power law proposed in the original work of Stewart et al. (1998), Adamidis and Madabhushi (2015), and Gao and Vulpe (2022) at reference concentration C_{ref}. The obtained determination coefficients from the generic relationship closely match those corresponding to fit-for-purpose power laws, as listed in Table 4. This suggests that the generic fitting expression can be successfully calibrated based on the determination of μ_{ref} at C_{ref} for any batch of HPMC, provided it is of a similar type as those explored in

this study. This approach eliminates the need for an elaborate calibration study examining the viscosity at many different concentrations, thereby saving time and resources while still obtaining a high-quality fitting expression.

4.3. Effect of HPMC type on pore pressure development during dynamic pile installation

As highlighted in Section 4.1, HPMC-based viscous fluids show shear thinning behavior due to the alignment of the cellulose polymers in the fluids at higher shear rates. This phenomenon results in a decrease in apparent viscosity with increasing shear rates. This behavior is amplified as higher viscosity grades of HPMC are used and the concentration of the solution increases, as demonstrated in Fig. 6. The implications of this behavior on the results of dynamic centrifuge tests are not fully understood. However, these effects likely play a role in the generation and dissipation of pore pressures and, therefore, through effective soil stresses, influence the soil behavior.

An example of a centrifuge experiment where the shear thinning of viscous fluid should be accounted is dynamic pile installation. In this work, three of such centrifuge tests are conducted on samples saturated with different fluids. Specifically, samples are saturated with water (H_2O), an aqueous solution of Methocel F50, and an aqueous solution of Methocel F4M. For F50 and F4M the viscosity of the viscous fluids amounts to 45.3 mPa·s and 48.3 mPa·s at the normalizing shear rate of 10 and 5.01 s^{-1}, respectively. Key parameters of the tests are summarized in Table 2. Further information on the test execution is presented in Section 3. Figure 9 shows the evolution of the normalized pile embedment, L/D_P, associated with each experiment. In the legend, the saturation medium for each experiment is listed.

From Fig. 9, it is observed that combined self-weight penetration during 1g and Ng is similar for all samples, indicating consistent sample preparation between tests. However, significant differences are observed in terms of the rate of self-weight settlement. The most notable difference between the water-saturated and viscous fluid samples is the settlement rate during the 1g self-weight installation phase (marked by vertical dashed lines labeled as $t = t_{1g}$ and $t = t_{1g} + 292$ s in Fig. 9), which occurs significantly faster in the water-saturated sample. The difference in permeability between samples underlies this observation. As the pore fluid viscosity is approximately 50 times higher than that of the water-saturated sample, the permeability is reduced by 50 times. Under 1g conditions, this reduces the migration speed of the pore fluid through the granular matrix. As the driving mechanism behind the pile's sinking is cavity expansion (Salgado et al. 1997), this process is controlled by the flow velocity of the pore fluid, which in turn dictates the deformation rate of the soil medium. The higher viscosity of the pore fluid substantially slows the flow speed. This results in a slower pile settlement rate for samples saturated with viscous fluid.

In contrast, the pile settlement rate under self-weight is similar for all samples at *Ng* conditions, which is marked by the vertical dashed lines and labeled as $t = t_{Ng}$ and $t = t_{Ng} + 161$ s in Fig. 9. Although the inherent differences between samples remain, they do not influence the experimental observations to the same extent as under 1g conditions. Additionally, as the centrifuge accelerates to 50 *g*, the loading conditions experienced by the pile and soil model evolve similarly across all samples. This triggers a sequence of small bearing failures, which gradually accumulate additional self-weight penetration over time. However, these events are not prolonged enough to cause significant deviations in pile settlement between the samples. This effect is further exacerbated by the continuous increase in acceleration levels, which keeps the system unbalanced during spin-up. Equilibrium conditions are only reached once the target acceleration of 50 *g* is achieved.

After the self-weight installation of the pile, a series of single blows dynamically drives the pile to its final embedment level. For each blow, a rapid increase in the pile-embedment ratio is observed at the moment of impact. It is evident that the penetration increments are larger for the water-saturated sample, thus resulting in a larger cumulative penetration rate. This behavior is linked to differences in drainage conditions under centrifugal acceleration, where the water-saturated sample has a larger permeability compared to the viscous fluid samples. Under dynamic conditions, this results in less pronounced and shorter-lived deviations in the pore pressure field. As the system response is predominantly drained, the effective stresses depend mainly on the hydrostatic back-pressure.

This is not the case for the viscous fluid-saturated samples, which have reduced permeability and are more likely to exhibit undrained or partially drained behavior under dynamic loading. Consequently, effective stresses fluctuate in response to a constrained volumetric deformation, leading to more pronounced deviations from the hydrostatic back-pressure. In these samples, the reduced pile penetration rate suggests that the observed decrease in pore pressure is likely caused by constrained dilative behavior around the pile. Under undrained conditions, volumetric changes cannot occur, a constrained dilative response is therefore associated with a reduction in pore pressure and increase in effective stress.

According to critical state soil mechanics, a constrained dilative response is expected when the stress state lies below the critical state line in the void ratio-effective stress (e-p′) space. Given the samples' high relative density such a response is plausible (see Table 2). The extent of constrained dilation, and thus the magnitude of negative pore pressures, is influenced by the confining stress. For a fixed void ratio, deeper soils under higher effective stress move closer to the critical state line and may exhibit a reduced dilation or even a contractive behavior. However, the current data do not provide evidence of a depth-dependent soil response during pile driving (see Fig. 10). For the water-saturated sample, the soil response is purely contractive, whereas for the F50 and F4M samples the response depends primarily on the relative position of the PPT to the pile's tip, showing a dilative response below the tip and a contractive response along the shaft. It is plausible that the penetration range explored in this study is insufficient to fully resolve the influence of the confining stress with depth. Simulating deeper penetration or a higher

Fig. 9. Installation sequence of the model piles for different saturation media. Vertical lines segment the *x*-axis segment into uneven time intervals to highlight the contribution to the embedment depth of each installation phase. This includes (i) 1g self-weight penetration, starting at t_{1G}; (ii) Ng self-weight penetration, starting at t_{NG}; (iii) penetration per blow, starting at t_{Bn}, where n denotes the blow number.

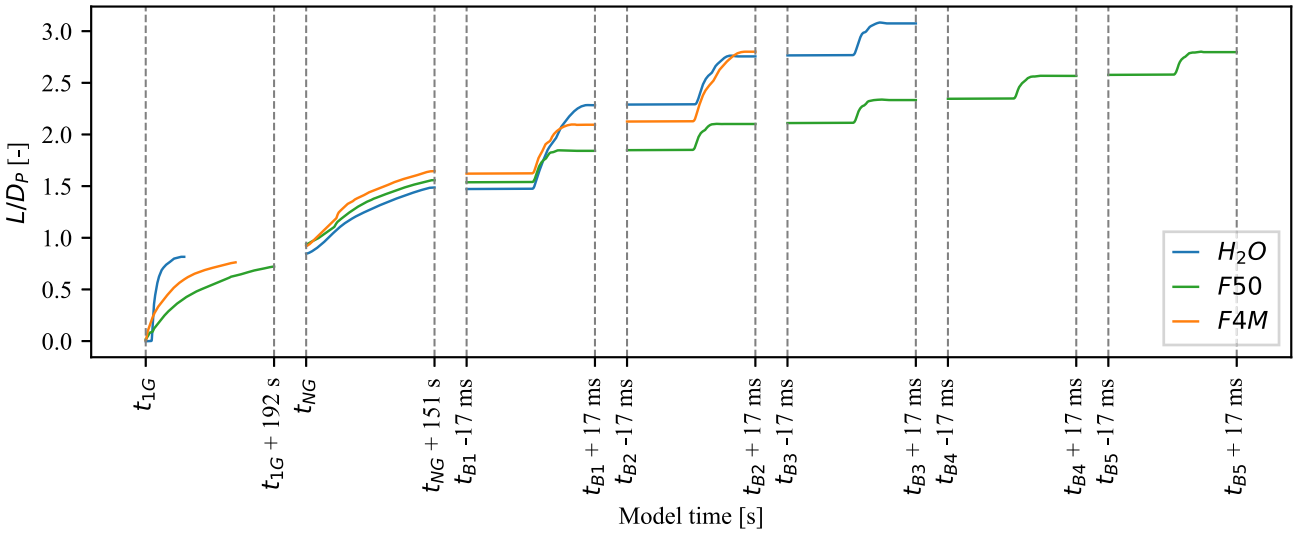

Fig. 10. Excess pore pressure ratio, R_u versus model time for all blows conducted in the samples saturated with H_2O, F50, and F4M. Pressures are recorded by three pore pressure transducers (PPTs) located at D_P (shallow), $2D_P$ (middle), and $3D_P$ (deep) relative to soil surface level of the sample. All PPTs are positioned at a radial distance of D_P relative to the pile centroid. Numbers on the color bars indicate the relative (vertical) distance between the pile embedment and the respective sensor soil horizon, followed by the blow count, shown as (B*n*), where n denotes the blow number. Positive values are used when the $L \leq S$. Negative values correspond to $L > S$. Light-gray shaded areas indicate the time intervals during which the pile is moving.

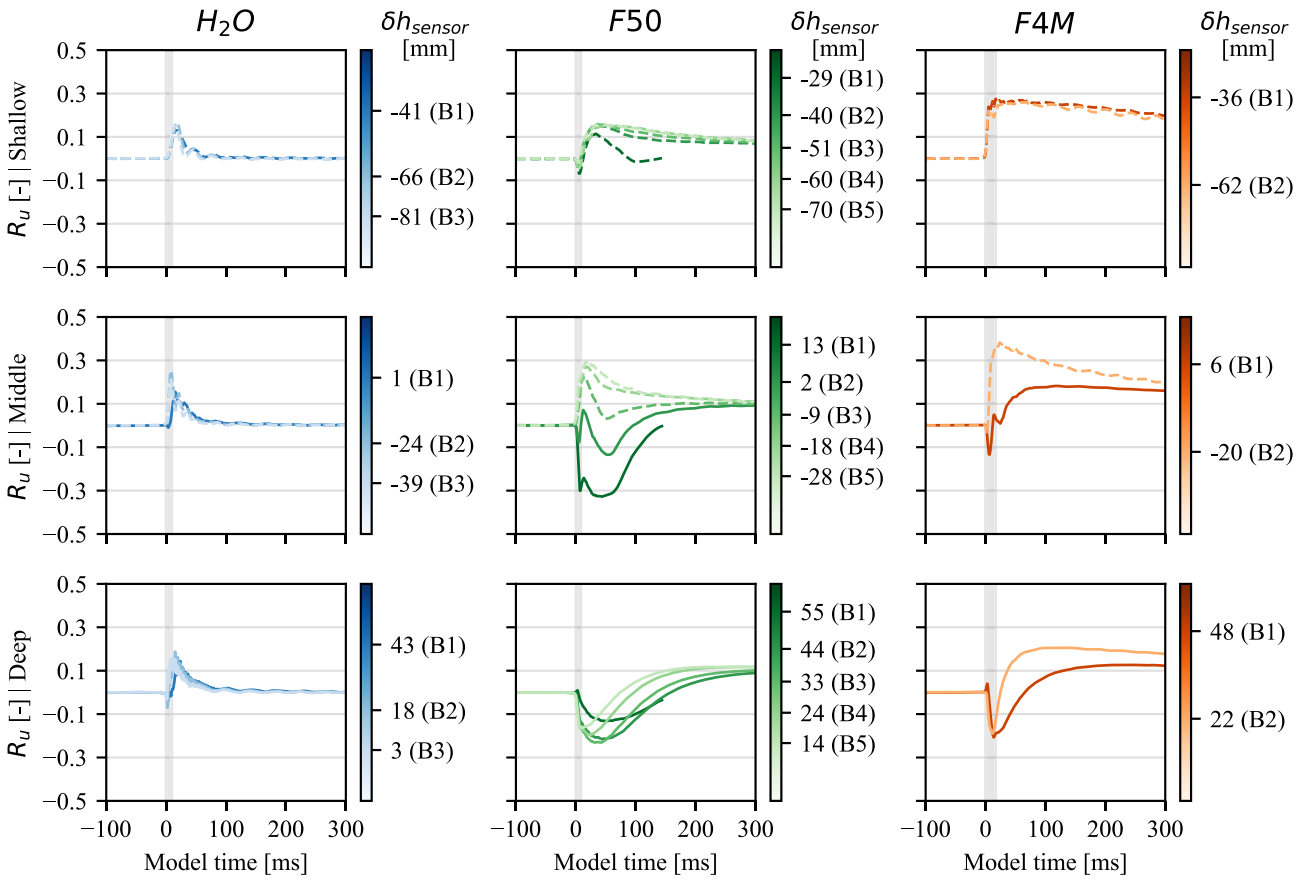

Fig. 11. Excess pore pressure ratio, R_u, as a function of the incremental pile displacement for each blow conducted in the samples saturated with H_2O, F50, and F4M. Pore pressure transducers (PPTs) positions and legend configuration are the same as presented in Fig. 10.

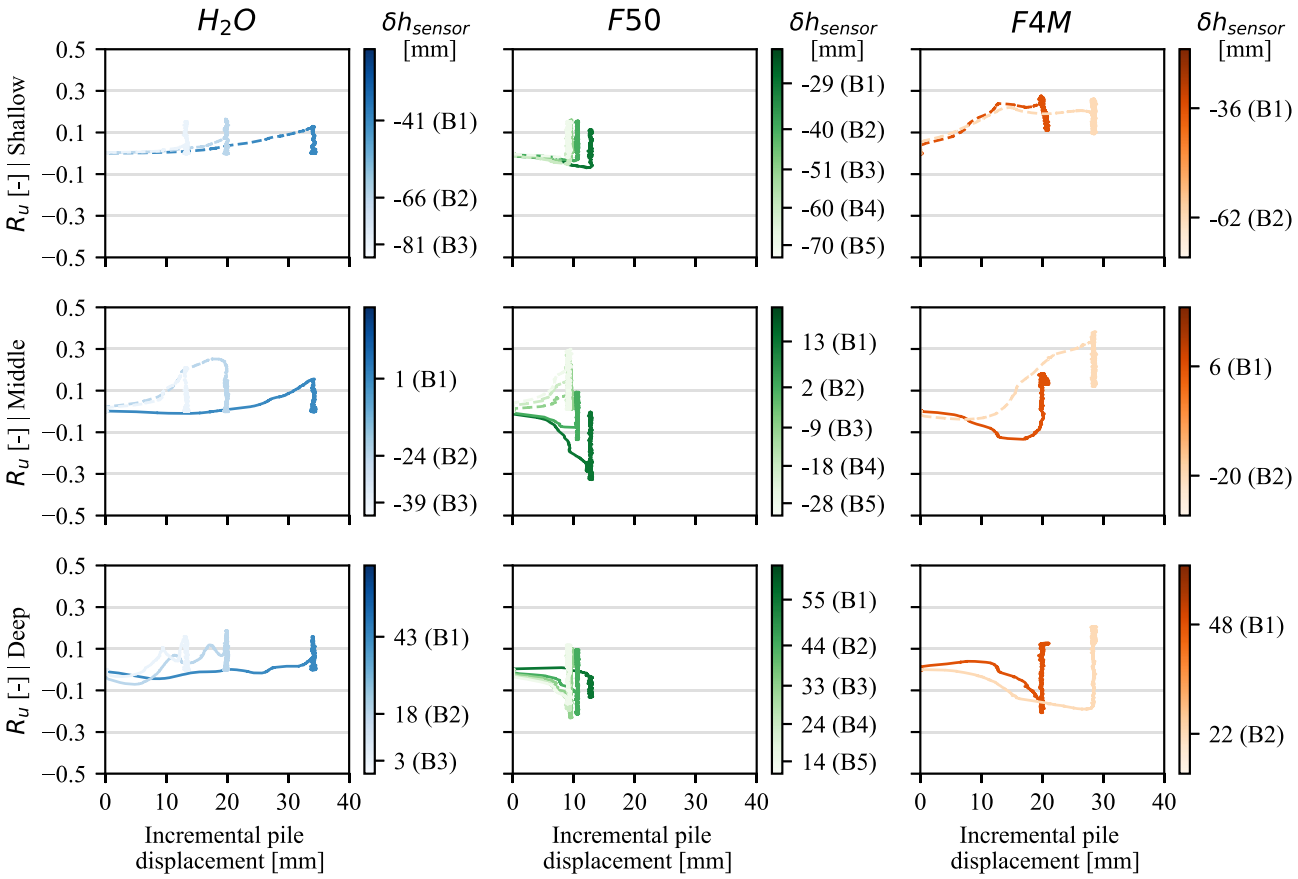

stress state (e.g., by increasing centrifuge acceleration) could help clarify the influence of confining pressure on the overall soil response. However, this lies beyond the scope of the present study.

To illustrate the saturated soil response, Figs. 10 and 11 show the excess pore pressure ratio, R_u, during the dynamic phase of the installation process, as a function of model time and incremental pile displacement per blow, respectively. R_u is defined in eq. 7 as the difference between the dynamic pore pressure, p_{dyn}, and the hydrostatic back-pressure, p_{stat}, over the vertical effective stress under hydrostatic conditions, $\sigma'_{v,stat}$, at the respective sensor depth.

$$R_u = \frac{p_{dyn} - p_{stat}}{\sigma'_{v,stat}} \quad (7)$$

Figure 10 displays the pore pressure response between the 0.1 s leading up to the dynamic event and the subsequent 0.3 s. It is observed that for both the F50 and F4M samples, negative R_u values are recorded from the moment of impact during several blows. This observation supports the interpretation of a constrained dilative soil response, along with a corresponding reduction in settlement due to the development of disadvantageous stress conditions.

For all tests, p_{dyn} is recorded at 100 kHz using a triggered measurement initiated at the moment of impact. This 1 s burst measurement includes a pre-trigger interval, allowing part of the data leading up to the dynamic event to be captured. It is important to note that the response time of the PPTs is 1 ms, which intrinsically limits the effective measurement frequency to 1 kHz. As the impact duration ranges from approximately 8 to 13 ms (illustrated by the shaded band in Fig. 12), roughly 8–13 valid measurement points are recorded during the moment of impact. While the measurement density during the dynamic event is limited, it is considered sufficient to capture the global evolution of pore pressures, particularly during subsequent dissipation.

Figures 10 and 11 present the evolution of the excess pore pressure ratio, R_u, as measured by the PPTs installed at D_P, $2D_P$, and $3D_P$ from the surface, as a function of model time and incremental pile displacement per blow, respectively. In these figures, the PPT installation depths are labeled as "shallow", "middle", and "deep", highlighting the increasing distance between the sensor and the soil surface. The color bars in each subplot indicate the vertical distance, δh_{sensor}, defined as the difference between L, and the sensor soil horizon, S, expressed in millimeters. A positive δh_{sensor} ($L < S$) means that the PPT is located above the pile tip, with this distance increasing progressively with installation depth. Conversely, a

Fig. 12. Pile velocity (left *y*-axis) and shear rate (right y-axis) profiles during the dynamic installation of the model piles for different saturation media, as a function of model time. Each shaded line represents one blow, while the black solid lines show the average velocity and shear rate profiles for all blows, $\bar{B}$. Horizontal dashed lines denote the mean shear rate, $\bar{\dot{\gamma}}$, for $\bar{B}$. The shear rate is computed based on eq. 8.

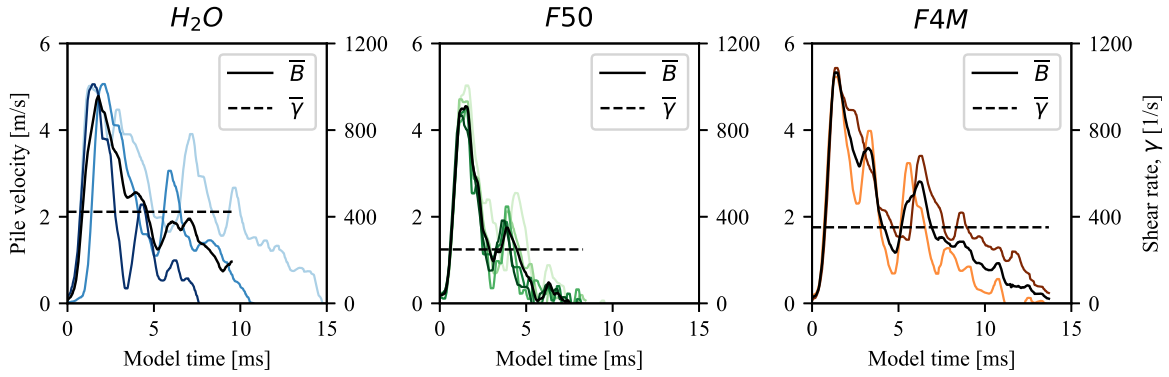

negative δh_{sensor} ($L > S$) indicates that the PPT is below the pile tip, meaning the pile is moving towards it. To distinguish these cases, dashed lines are used when $\delta h_{\text{sensor}} > 0$, whereas solid lines are used when $\delta h_{\text{sensor}} \leq 0$. Next to the color bar, the value of δh_{sensor} is followed by (Bn), where n denotes the blow number.

Starting with the data from the water-saturated model in Fig. 10, it is evident that, despite the enhanced soil permeability at model scale, the response is not fully drained. A fully drained response would involve instantaneous pore pressure dissipation and no gradual pressure fluctuations over time, which is not observed here. For all three measuring depths, the peak R_u value occurs at the end of pile displacement and dissipates within a comparable timeframe (as shown in Fig. 10). Figure 11 further shows that R_u increases monotonically to an extreme value of approximately 0.1 by the end of the pile movement. This trend is consistent across all PPTs and blows.

The undrained response is more pronounced in the viscous-fluid models. Both models show that larger R_u extremes and dissipation times exceed those in the water-saturated sample by more than an order of magnitude. This confirms that using water as a pore fluid increases apparent soil permeability in centrifuge modelling, while viscous fluids reduce it. As with the water-saturated model, the extreme R_u value in the F4M test occurs during pile movement. In the F50 test, however, the extreme is reached after the pile stops. Figure 11 shows that, for blows 1 and 2, the middle and deep sensors record peak R_u values after the pile has reached its final position.

Another key difference between the water-saturated and viscous-fluid models lies in the initial R_u response. In the water-saturated model, the initial response is consistently positive across all sensors and blows, indicating a uniform increase in pore pressure relative to hydrostatic levels, regardless of sensor depth or pile position. In the viscous-fluid models, the sign of the initial R_u response varies between sensors and blows, resulting in a heterogeneous pore pressure distribution. It is believed that due to reduced drainage in the viscous-fluid models, localized pressure changes are preserved. In contrast, similar fluctuations likely dissipate too quickly to be observed in the water-saturated model. As a result, the water-saturated response is dominated by net densification, and all sensor time histories appear similar (Fig. 10).

The effect of net densification is also observed in the viscous-fluid models. After approximately 300 ms, all sensors register a positive R_u value, independent of blow number. These differences indicate that centrifuge tests using water as a pore fluid may not accurately replicate prototype behavior in conditions where soil permeability is low or loading rates are high.

Upon further inspection of Figs. 10 and 11, the sign of R_u correlates with the sensor position (relative to the pile tip). Generally, a negative R_u, that is a decrease from p_{stat}, is recorded when $S > L$. An additional observation from Fig. 11 is that pore pressure tends to change monotonically during pile movement. This suggests that the soil experiences purely constrained contraction or dilation, with no transitional behavior (such as contractive turning into dilative, or vice versa) observed.

Judging by the response of the deep PPT in Fig. 10 (located at $3D_P$ below the soil surface), constrained dilation appears most pronounced at a distance of 75% to 100% of D_P beneath the pile tip. Furthermore, it is observed that R_u tends to be negative as long as the sensor is below the pile tip, indicating that the local pore pressure is below p_{stat}. A trend reversal is observed roughly when the pile embedment coincides with the sensor depth, i.e., $L = S$. As the distance increases further due to continued pile penetration, the pore pressure increasingly exceeds p_{stat}, before stabilising at approximately $0.1R_u$ at roughly 300 ms after impact. As the pore pressures tend to be below p_{stat} at impact, the effective stresses increase, particularly those at and below the pile tip. This results in less favourable driving conditions, thereby reducing the pile penetration rate. This effect likely underlies the observed divergence of the penetration curves in Fig. 9.

The location dependency of the sign of R_u is likely related to the predominant loading conditions in different zones surrounding the pile. Below the pile tip. there is a rapid increase in the compressive stresses at the moment of impact, which

leads to the formation of a "nose cone" (White and Bolton 2001). As the pile progresses through the soil body, the soil experiences high shear loading along the edge of the nose cone. The associated plastic shear deformations lead to the generation of excess pore pressures. Provided that the soil relative density is high, the soil experiences constrained dilation. This reduces the pore pressures locally, thus resulting in negative R_u values.

Along the pile shaft, soil is sheared cyclically, causing the interface layer to contract progressively over the full installation sequence (White and Lehane 2004; White 2005). Due to the contraction of the interface layer, soil in the far field experiences elastic relaxation (Basu et al. 2014). Shear (S-) waves radiating from the pile shaft induce shear in the soil skeleton, leading to a contractive response that increases pore pressures in the far field. This contraction accumulates over the subsequent blows and ultimately results in the densification of the soil surrounding the pile under the effects of consolidation. Sample densification was observed as a lowering of the entire soil surface inside the strongbox by approximately 3 mm over the full installation sequence.

As the majority of the soil volume undergoes net contraction, localized effects such as the negative R_u values beneath the pile tip are ultimately replaced by positive R_u values as pressures equalize prior to dissipation. This effect is clearly visible in Fig. 10, where for all pore fluids, the PPTs register positive R_u values after pressure equalization (but before full dissipation). The equalization of the pressures throughout the instrumented depth happens concurrently with the first dissipation of excess pore pressures towards the free drainage boundary at the top of the sample.

The global evolution of pore pressures resembles those of Hölscher et al. (2012), who performed rapid load tests on piles installed in saturated sand in the centrifuge, using displacement amplitudes up to $0.1D_P$ and comparable to this study. Though the nature of the prolonged blow installation method is more dynamic, as the pile's penetration velocity is roughly two orders of magnitude larger, Hölscher et al. (2012) found a similar pore pressure response surrounding the pile during the penetration phase. Sensors in the field of travel demonstrated a pronounced reduction during the downward movement of the pile, while sensors in the periphery of the pile recorded positive excess pore pressures. The overall response of the medium-dense sample was contractive, similar to this study.

For the viscous-fluid models, full dissipation of pore pressures is achieved within 1–1.5 s after the dynamic event. This is an important finding, as it illustrates that excess pore pressures in dense sand could be sustained for 50–75 s at the prototype scale. Pore pressures may therefore accumulate between blows if the driving frequency is high enough. Albeit a different dynamic installation method was used, the latter has been proposed as a potential cause for divergence between driveability predictions and recorded installation profiles for the installation of large diameter piles in dense sand (Cathie et al. 2020). Since the actuator requires a manual reset between blows, a continuous pore pressure log for the full installation sequence is unavailable in this study. Further developments in the installation hardware should facilitate the exploration of this research avenue in the future.

To estimate the influence of shear thinning on the system response, the average shear rate at the interface layer is computed by evaluating the quotient of the pile velocity, v_P, and the shear band thickness, t_i, as illustrated in eq. 8.

$$\dot{\gamma}_{soil} = \alpha \frac{v_P}{t_i} \tag{8}$$

The resulting quotient is multiplied by a slip coefficient, α, which accounts for slip between the pile and the surrounding soil, assuming that 20% of the pile movement is transferred to the surrounding soil ($\alpha = 0.2$). A discrete element model of the pile–soil interface was used to inform the selection of α. The equivalent interface layer thickness, t_i, is approximated as $8{\sim}d_{50}$, in line with the experimental observations of DeJong et al. (2003) for silica sand at high cumulative displacements. This assumption was also validated using DEM. For simplicity, contraction of the shear band is not considered. The resulting shear rates are plotted in Fig. 12. Shear rates reach extremes of up to 1000 s^{-1} independent of the saturation medium. This is logical as the pile initial velocity is imposed by collision dynamics; it is only afterwards that the effect of soil resistance becomes apparent in the displacement process.

As the duration of the dynamic event is between 8 and 13 ms (Fig. 12), during which the pile penetration rate varies significantly, shearing conditions around the pile are irregular and non-steady. For this reason, the effect of shear thinning on the pore fluid viscosity is estimated based on the mean shear rate, $\overline{\dot{\gamma}_{soil}}$, calculated from the average shear rate profiles, $\bar{B}$, shown as solid black lines in Fig. 12. It is clear that $\overline{\dot{\gamma}_{soil}}$ for water is roughly doubled compared to the experiment with F50, while F4M is in the middle of this range. It therefore seems that the presence of viscous fluid not only influences the displacement amplitude of the pile but also affects the mean penetration rate. Since $\overline{\dot{\gamma}_{soil}} < \dot{\gamma}_{max}$ (as used for the rheological characterization of the fluids in Section 4.1), the absolute reduction in viscosity is quantitatively evaluated.

Based on the results presented in Section 3, the associated reduction equals 5% and 20% for F50 and F4M, respectively. However, it is expected that the instant at which shear thinning effects are most detrimental to the installation response is when the pile penetration rate is the highest. The resulting reduction in viscosity improves drainage properties, facilitating soil particle movement and pile penetration, though a fully drained state is not reached. This is consistent with the pile penetration data (Fig. 9), which shows that the model saturated with F4M exhibits behavior intermediate between the water-saturated and F50 samples. Overall, the reduced influence of constrained dilation for models saturated with water and F4M also leads to a softer soil response. This is why the impact duration, which is shown on the horizontal axis of Fig. 12, is the largest for the water-saturated sample, followed by the F4M sample. The influence of reduced rate effects, e.g., viscous dampening (Huy et al. 2005), arguably offsets part of the increased penetration resistance due to excess pore pres-

sure development when using a viscous fluid, though this is not directly appreciable from the experimental data.

Referring to Fig. 10, a key distinction lies in the generation of negative pore pressure, where the response is more immediate for F4M when compared to F50. In the case of F50, the minimum pore pressure is recorded after pile movement has ceased, whereas for F4M, the peak occurs while the pile is still in motion (similar to the water-saturated sample). Notably, the magnitude of the minimum pore pressure is similar (-0.15 to $-0.20R_u$) between both tests, provided the distance between the pile tip and the sensor (as listed next to the color bars) is comparable. The position of the PPTs relative to the pile likely play a role in this observation. As viscosity decreases under shear, it facilitates faster deformations in shear zones and increases the migration velocity of the pore fluid. For F4M, this results in the peak excess pore pressure occurring during pile movement. In this case, it is expected that the recorded extreme is close to the true extreme that was reached during pile displacement. It is questionable whether this is also the case for F50, which is less prone to shear thinning. As a result, the pore fluid retains a higher viscosity under shear, leading to slower fluid movement and a delayed pore pressure response. Consequently, the extreme pore pressure for F50 is only recorded after the pile stopped moving and the generative event has ended. In turn, pressures might have partially diffused, meaning that the recorded extreme for the F50 experiment might be lower than the true extreme. The effect of constrained dilation during pile displacement might therefore be underestimated based on the PPT readings alone. This arguably explains why, despite similar effective stresses based on the pressure readings in Fig. 10, pile displacement deviates considerably between the F50 and F4M tests in Fig. 9.

Differences in the pore pressure response between the F50 and F4M tests persist beyond the R_u extrema. As shown in Fig. 10, the dissipation rates, indicated by the slope of the R_u versus time curve, differ between the viscous fluid tests as long as a pressure gradient exists within the sample. This gradient is evidenced by differing pressure readings from the three PPT sensors at a given time and is believed to drive fluid migration through the soil model. The migration rate is higher in the F4M experiment than in the F50 experiment. This suggests that shear-thinning effects influence pore pressure dissipation even after dynamic loading has ceased. In this context, shear likely arises from frictional resistance as the pore fluid moves through the soil matrix. This process appears to delay the re-establishment of LVR viscosity, resulting in different pressure equalization times: approximately 0.3 s for F50 and 0.1 s for F4M. As the pressure gradients diminish, the behavior of both viscous fluids converges, yielding similar excess pore pressure dissipation rates after 0.3 s.

In summary, shear thinning significantly influences the generation and dissipation of excess pore pressure in dynamic centrifuge modelling. These effects are localized to regions of the sample experiencing the highest shear rates, notably around the pile's nose cone and along the pile shaft. Given the role these areas play in mobilizing soil resistance, shear thinning influences the total driving resistance, leading to diverging pile penetration profiles between tests. To some surprise, the response of the water saturated sample in the centrifuge is not fully drained. Yet, significant differences remain in relation to the response obtained from samples saturated with a viscous fluid. For the dynamic installation case investigated in this work, it is therefore the least suitable alternative out of the three options. Nonetheless, significant differences are also observed between tests using F50 and F4M, despite both fluids having similar viscosities within their respective LVR. The reduction in viscosity for F4M also facilitates greater pile penetration, although it remains less than that seen with water as the pore fluid. The corresponding soil stiffness is lower for F4M due to quicker fluid movement and faster soil deformation. Given these observations, it is advisable to account for shear thinning effects when selecting a viscous fluid for dynamic centrifuge studies in saturated sand. Other dynamic centrifuge models, like shaking table tests (Kutter et al. 2018), would require further consideration of the LVR span for the selected viscous fluid. The results presented in this work point to the strong link between the acting shear rate and the dissipation of excess pore pressures, confirming the estimates of Adamidis and Madabhushi (2015) for earthquake modelling and raising awareness on the careful selection of a scaled pore fluid.

5. Conclusions

This study formulates a standardized protocol for preparing aqueous solutions of various HPMC types and evaluates their rheological behavior and performance for the case of a dynamic pile installation in the centrifuge. HPMC viscous fluids exhibit a shear-thinning behavior to varying degrees, depending on their molecular weight and concentration. These effects reduce the LVR, defined as the range of shear strain rates over which viscosity remains constant. To select an appropriate fluid for a centrifuge modelling campaign, the LVR should be compared against the expected shear rate range, as also suggested by previous studies. To facilitate the preparation of viscous fluids, a modified power-law model, calibrated relative to a single reference viscosity, is proposed, relating HPMC concentration with a target viscosity. This approach accounts for fabrication tolerances and chemical variability between HPMC types by introducing a reference viscosity at a predefined concentration as one of the calibration parameters. As demonstrated in this work, the model successfully unifies results from this study with those of previous works and significantly reduces the need for extensive rheological testing. The accompanying preparation methodology improves reproducibility across studies and simplifies implementation by clearly defining the required equipment and mixing procedures.

Centrifuge tests confirm the utility of using viscous fluids for dynamic pile installation, showing clear differences compared to a water-saturated sample. The use of a shear thinning fluid accelerates the pore pressure dissipation and alters the effective stress state during dynamic loading. For samples saturated with a viscous fluid, negative excess pore pressures develop beneath the pile tip, increasing the effective stresses and reducing the pile penetration rates relative to the water-saturated model. While the magnitude of pressure

reduction is similar, the timing of the R_u peaks differ. For the shear thinning fluid, HPMC-F4M, R_u peaks during pile displacement (similar to the water-saturated sample), whereas for the longer LVR fluid, HPMC-F50, they are recorded after the pile movement has ceased. Nevertheless, the recorded R_u peaks in F50 may be underestimated, due to the placement of the PPTs within the sample. Penetration data offer a more reliable indicator of driving conditions and suggest greater soil resistance during installation in the sample saturated with F50. Moreover, constrained dilation likely contributes to the higher driving resistance, slowing soil deformation and reducing the overall penetration rate. After the dynamic event, pressure equalization proceeds under a residual pressure gradient within the sample. Equalization occurs approximately 70% faster in samples saturated with F4M than those saturated with F50. It is likely that shear-thinning effects still influence fluid behavior during this phase, as the fluid experiences resistance while migrating through the granular structure. Once pressures equalize, dissipation rates converge for both fluids, being consistent with their similar LVR viscosities.

When selecting an HPMC viscous fluid for dynamic centrifuge modelling, specifically in low permeable media and at high shear rates, shear-thinning effects must be considered. HPMC with a lower viscosity grade is less prone to shear thinning and are thus better suited for highly dynamic applications. For static or quasi-dynamic tests, higher-viscosity grades may offer advantages in cost and stress equivalence, due to their density being closer to that of water. In either case, the unified relationship between concentration and viscosity together with the standardized preparation protocol presented here remove logistical barriers and enhance the practical use of viscous fluids in geotechnical centrifuge modelling. The results reported in this work demonstrate that the saturated response of a sample can vary significantly depending on the choice of pore fluid. In particular, differences in shear-thinning behavior between aqueous solutions of HPMC underscore the importance of selecting the appropriate HPMC type based on the expected shear rates during an experiment. While estimating these shear rates in advance may not always be straightforward, the authors are confident that increased awareness of the implications of shear thinning on centrifuge modelling results will enhance the quality and and reliability of future investigations into saturated soil dynamics and soil–structure interactions.

Acknowledgements

This work is supported by a research grant from Topsector Energie (reference TSE-19-04-01-Hernieuwbare energieproject). The authors would like to thank their industrial partner, IQIP, for their constructive feedback and invaluable suggestions.

Article information

History dates

Received: 7 March 2025
Accepted: 16 September 2025
Accepted manuscript online: 1 October 2025
Version of record online: 27 November 2025

Copyright

Data availability

Data generated or analyzed during this study will be available on TU Delft's 4TU Repository (https://data.4tu.nl/) and released after manuscript acceptance.

Author information

Author ORCIDs

T.O. Quinten https://orcid.org/0009-0007-8391-8149
A.A. Askarinejad https://orcid.org/0000-0002-7060-2141
K. Gavin https://orcid.org/0000-0002-0741-1115
M.A. Cabrera https://orcid.org/0000-0002-9236-8130

Author notes

Miguel Cabrera served as Associate Editor at the time of manuscript review and acceptance; peer review and editorial decisions regarding this manuscript were handled by another editorial board member.

Author contributions

Conceptualization: AAA, MAC, TOQ
Formal analysis: TOQ
Funding acquisition: KG
Investigation: TOQ
Methodology: TOQ
Project administration: AAA, KG, MAC
Resources: AAA, KG
Supervision: AAA, KG, MAC
Visualization: TOQ, MAC
Writing – original draft: TOQ
Writing – review & editing: AAA, KG, MAC

Competing interests

The authors declare that they have no competing interests.

References

Adamidis, O., and Madabhushi, G.S.P. 2015. Use of viscous pore fluids in dynamic centrifuge modelling. International Journal of Physical Modelling in Geotechnics, **15**(3): 141–149. doi:10.1680/jphmg.14.00022.

Allard, M., and Schenkeveld, F. 1994. The Delft Geotechnics model pore fluid for centrifuge tests. Centrifuge, **94**: 133–136.

Anton Paar 2024. Avoid measurement errors in rheometry. Available from https://wiki.anton-paar.com/en/avoid-measurement-errors-in-rheometry/ [accessed August 22, 2025].

Askarinejad, A., Beck, A., and Springman, S.M. 2015. Scaling law of static liquefaction mechanism in geocentrifuge and corresponding hydromechanical characterization of an unsaturated silty sand having a viscous pore fluid. Canadian Geotechnical Journal, **52**(6): 708–720. doi:10.1139/cgj-2014-0237.

Basu, P., Koukidis, L., Prezzi, M., and Salgado, R. 2014. The mechanics of friction fatigue in jacked piles installed in sand. *In* Proceedings of the Geo-Congress 2014. *Edited by* M. Iskander, J. Garlanger and M. Hussein. American Society of Civil Engineers, Atlanta, Georgia, USA. pp. 546–557. doi:10.1061/9780784413265.

Bowman, E.T., Laue, J., Imre, B., and Springman, S.M. 2010. Experimental modelling of debris flow behaviour using a geotechnical centrifuge. Canadian Geotechnical Journal, **47**: 742–762. doi:10.1139/T09-141.

Cabrera, M.A., Kailey, P., Bowman, E., and Wu, W. 2018. Effects of viscosity in granular flows simulated in a centrifugal acceleration field. *In* Proceeding of the 9th international conference on phyical modelling in geotechnics 2018 (ICPMG 2018). *Edited by* A. McNamara, S. Divall, R. Goodey, N. Taylor, S. Stallebrass and J. Panchal. Taylor & Francis Group, London, UK. pp. 1075–1080. doi:10.1201/9780429438646-48.

Cabrera, M.A., Leonardi, A., and Peng, C. 2020. Granular flow simulation in a centrifugal acceleration field. Geotechnique, **70**(10): 894–905. doi:10.1680/jgeot.18.P.260.

Cathie, D., Jaeck, C., Ozsu, E., and Raymackers, S. 2020. Insights into the driveability of large diameter piles. ISFOG, **21**: 757–766.

DeJong, J.T., Randolph, M.F., and White, D.J. 2003. Interface load transfer degradation during cyclic loading: a microscale investigation. Soils and Foundations, **43**(4): 81–93. doi:10.3208/sandf.43.4_81.

Dewoolkar, M., Ko, H.Y., Stadler, A., and Astaneh, S. 1999. A substitute pore fluid for seismic centrifuge modeling. Geotechnical Testing Journal, **22**(3): 196–210. doi:10.1520/GTJ11111J.

Gao, J., and Vulpe, C. 2022. School of engineering preparation of viscous pore fluid for use in centrifuge testing using methocel F450 food gradient. Technical report, University of Western Australia. doi:10.26182/mgz4-zz21.

Garnier, J., Gaudin, C., Springman, S., Culligan, P., Goodings, D., Konig, D., et al. 2007. Catalogue of scaling laws and similitude questions in geotechnical centrifuge modelling. International Journal of Physical Modelling in Geotechnics, **7**(3): 01–23. doi:10.1680/ijpmg.2007.070301.

Goodings, D. 1984. Relationships for modelling water effects in geotechnical centrifuge models. *In* Symposium on the application of centrifuge modelling to geotechnical design. pp. 1–24.

Hölscher, P., Van Tol, A.F., and Huy, N.Q. 2012. Rapid pile load tests in the geotechnical centrifuge. Soils and Foundations, **52**(6): 1102–1117. doi:10.1016/j.sandf.2012.11.024.

Huy, N., Dijkstra, J., Van Tol, A., and Hölscher, P. 2005. Influence of loading rate on the bearing capacity of piles in sand. *In* Proceedings of the 16th International Conference on Soil Mechanics and Geotechnical Engineering. Millpress Science Publishers/IOS Press, Osaka, Japan. pp. 2125–2128. doi:10.3233/978-1-61499-656-9-2125.

Keetels, G.H., Chauchat, J., and Breugem, W.P. 2023. Role of turbulent kinetic energy modulation by particle-fluid interaction in sediment pick-up. Journal of Fluid Mechanics, **955**.

Kementzetzidis, E., Wang, H., Marino, M., Askarinejad, A., da Silva, A.P., Elkadi, A.S., and Pisan, F. 2023. Monopile-sand interaction under lateral cyclic loading: simulation of centrifuge test data using a cyclic 1D p-y model. *In* 9th International SUT Offshore Site Investigation Geotechnics Conference Proceedings "Innovative Geotechnologies for Energy Transition". Society of Underwater Technology. pp. 1083–1090. doi:10.3723/GLCF8450.

Khalifa, A., Garnier, J., Thomas, P., and Rault, G. 2000. Scaling laws of water flow in centrifuge models. *In* Int. Symp. on Physical and Testing in Environmental Geotechnics.

Kutter, B.L., Carey, T.J., Hashimoto, T., Zeghal, M., Abdoun, T., Kokkali, P., et al. 2018. LEAP-GWU-2015 experiment specifications, results, and comparisons. Soil Dynamics and Earthquake Engineering, **113**(May 2017): 616–628. doi:10.1016/j.soildyn.2017.05.018.

Maghsoodi, S., Wang, H., Konstadinou, M., Pisanò, F., and Askarinejad, A. 2022. Monopile improved design through advanced cyclic soil modelling: Project Report 1—Geba sand laboratory tests. Technical report.

Maghsoudloo, A., Askarinejad, A., de Jager, R., Molenkamp, F., and Hicks, M. 2018. Experimental investigation of pore pressure and acceleration development in static liquefaction induced failures in submerged slopes. *In* Proceedings of the 9th International Conference on Physical Modelling in Geotechnics (ICPMG 2018). *Edited by* A. McNamara, S. Divall, R. Goodey, N. Taylor, S. Stallebrass and J. Panchal. Taylor & Francis Group, Londen, UK. pp. 987–992. doi:10.1201/9780429438646-34.

McMullen, R.L., Ozkan, S., and Gillece, T. 2022. Physicochemical properties of cellulose ethers. Cosmetics, **9**(3). doi:10.3390/cosmetics9030052.

Mezger, T.G. 2016. The Rheology Handbook: for users of rotational and oscillatory rheometers. 2nd ed. Vincentz Network, Hannover, Germany. doi:10.1515/9783748600367-009.

Quinten, T., Askarinejad, A., Gavin, K., Winkes, J., and Van Wijk, J. 2022. Designing PULSE and BLUE blow generators for experimental research in the geotechnical centrifuge. *In* Proceedings of the 11th International Conference on Stress Wave Theory and Design and Testing Methods for Deep Foundations (SW2022). pp. 1–9. doi:10.5281/zenodo.7151838.

Sadasivuni, K., Ponnamma, D., Kim, J., Cabibihan, J.J., and AlMaadeed, M. 2017. Biopolymer composites in electronics. Elsevier. doi:10.1016/c2014-0-04575-3.

Salgado, R., Mitchell, J.K., and Jamiolkowski, M. 1997. Cavity Expansion and Penetration Resistance in Sand. Journal of Geotechnical and Geoenvironmental Engineering, **123**(4): 344–354. doi:10.1061/(asce)1090-0241(1997)123:4(344).

Steedman, R.S., and Ledbetter, R.H. 1994. Centrifuge modeling of earthquake problems. *In* International Workshop on Remedial Treatment of Liquefiable Soils.

Stewart, D., Chen, Y.R., and Kutter, B. 1998. Experience with the use of methylcellulose as a viscous pore fluid in centrifuge models. Geotechnical Testing Journal, **21**(4): 365–369. doi:10.1520/GTJ11376J.

Struble, L., and Jiang, Q. 2004. Effect of air entrainment on rheology. ACI Materials Journal, (101): 448–456.

Terwindt, J., Star, W., and De Lange, D. 2020. Carboxymethylcellulose as a Newtonian viscous fluid for centrifuge modelling. *In* Proceedings of the 4th European Conference on Physical Modelling in Geotechnics. pp. 75–83.

The Dow Chemical Company, 2002. METHOCEL cellulose ethers, Technical Handbook. Technical report, The Dow Chemical Company, Staines, UK.

White, D. 2005. A general framework for shaft resistance on displacement piles in sand. *In* Frontiers in offshore geotechnics. Taylor & Francis. pp. 741–748. doi:10.1201/NOE0415390637.ch78.

White, D.J., Bolton, M.D.2001 and Springman, S. 2001. Observing friction fatigue on a jacked pile. *In* Proceedings of the Workshop on Constitutive and Centrifuge Modelling. *Edited by* Balkema, Rotterdam, Monte Verità, Switzerland.

White, D.J., and Lehane, B.M. 2004. Friction fatigue on displacement piles in sand. Géotechnique, **54**(10): 645–658. doi:10.1680/geot.2004.54.10.645.

Appendix A: Scaling principles of fluid flows in a centrifuge model

The coupled and complex interactions of fluid flow through granular media involve a competition between the inertial and viscous forces of both fluid and grains, along with the resultant diffusion driven by pressure gradients. Capturing this competition is fundamental for the appropriate scaling of a given prototype into a centrifuge model. Hereafter, quantities referring to the prototype are denoted with the subscript p, while those referring to the model are denoted with the subscript m. A scaling factor N is employed such that the model acceleration a is N times Earth's gravity, g: $a = Ng$ (Garnier et al. 2007). The scaling principles for centrifuge modelling propose addressing this challenge by focusing on matching the time scales for diffusion, dynamic, and kinetic processes.

Diffusion is characterized by Terzaghi's dimensionless time factor for one-dimensional consolidation, $T_v = C_v t/l^2$, where C_v is the soil coefficient of consolidation and l is a drainage distance. Here, $C_v = k/(m_v \rho g)$ is assumed to be a material parameter and hence to be the same between model and prototype, provided that the soil permeability k, the soil compressibility m_v, and fluid density ρ are common between both

Table A1. Scaling principles for fluid flow for diffusion, dynamic, and kinetic processes for two scenarios of scaling the fluid dynamic viscosity μ.

		$\square_m/\square_p$	
		$\mu_m = \mu_p$	$\mu_m = N\mu_p$
Diffusion	k	N	1
	C_v	1	N^{-1}
	t^{diff}	N^{-2}	N^{-1}
Dynamic	t^{dyn}	N^{-1}	N^{-1}
Kinetic	i	1	1
	k	N	1
	v	N	1
	t^{kin}	N^{-2}	N^{-1}

Note: $\square_m/\square_p$ denotes the scaling ratio between model m and prototype p. The reported scaling principles for kinetic processes are derived under the assumption of laminar flow conditions.

scales. In such a case, $T_{v,m} \equiv T_{v,p}$ and the time scale between model and prototype is simply related by the geometrical scaling $l_m = l_p/N$. Solving t from T_v leads to the diffusion time scaling $t_m^{\text{diff}} = t_p^{\text{diff}}/N^2$, meaning that the time required to diffuse or dissipate a given pressure gradient is N^2 times shorter in the centrifuge compared to the prototype. Note that k is a function of both soil and fluid in the form of $k = \kappa\rho g/\mu$, where κ is the soil intrinsic permeability, and μ is the fluid dynamic viscosity. Therefore, increasing μ while keeping all other properties constant leads to a modified consolidation coefficient $C_{v,m} = C_{v,p}/N$, hence extending the diffusion time to $t_m^{\text{diff}} = t_p/N$.

The scaling of convective processes include both dynamic and kinetic time scales, t^{dyn} and t^{kin}, respectively. A dynamic-driven process scales by the model acceleration $a_m = Na_p$, over a characteristic distance $l_m = l_p/N$. Hence, the dynamic time defined as $t^{\text{dyn}} = (l/a)^{1/2}$ leads to a scaling between model and prototype in the form of $t_m^{\text{dyn}} = t_p^{\text{dyn}}/N$, only matching the diffusion time t^{diff} when the fluid viscosity is scaled. This is one of the main reasons to use a viscous fluid in processes governed by both t^{diff} and t^{dyn}.

When scaling the kinetic time scale, it is important to ensure the similitude of the dominant flow regime of both grains and fluid. Failing to account for it might hinder the insight gained from the model (Goodings 1984). The theory behind this scaling has been formulated since the conception of centrifuge modelling as a simulation tool for geotechnical engineering. The works of Goodings (1984) and Khalifa et al. (2000) posited the modelling framework, focusing on the different flow regimes in granular media (i.e., laminar flow, turbulent flow). These flow regimes are conceptualized through dimensional analysis by simplifying the hydro-mechanical system by a characteristic length set by a reference grain diameter d, which is then related with a characteristic fluid velocity v, and a characteristic mass governed by the grain's density ρ_g. This analysis leads to two dimensionless number. The Reynolds number $\text{Re} = v\rho_g d/\mu$, which expresses the ratio between inertial and viscous forces, and Darcy's friction factor $\text{F}_\text{D} = igd/v^2$ capturing the ratio between the grains and fluid inertia. In the latter, i is the dimensionless hydraulic gradient marking an energy imbalance and flow direction. Note that the shear rate can be retrieved in both Re and F_D by assuming $\dot{\gamma} = v/d$.

In the framework presented by Khalifa et al. (2000), a laminar flow occurs when viscous forces dominate ($\text{Re} \lesssim 10$) and the fluid velocity can be expressed by Darcy's law, $v = ki$. Higher inertial forces transition the flow into a laminar nonlinear regime ($10 \lesssim \text{Re} \lesssim 100$) where i is better expressed by Forcheimer's relationship $i = av + bv^2$, where a and b describe energy losses due to viscous and inertial dissipation mechanisms, respectively. As the fluid and grains gain more inertia ($100 \lesssim \text{Re} \lesssim 800$), the flow enters a transitional regime with irregular flow patterns. Finally, inertia dominates the interactions above a certain limit and the flow is in a turbulent regime ($\text{Re} \gtrsim 800$). At this point, the fluid flow becomes highly irregular and leads to significant fluid drag forces (Keetels et al. 2023).

For simplicity, let us focus on the laminar regime and look at Darcy's law and scale the hydraulic gradient i. Here, two alternative interpretations are possible:

- **Alternative A**: Assume that $i = \Delta h/l$ is driven by a dimensionless loss-to-flow length ratio, where Δh is a water column height and l is a flow length. Here, increasing the model acceleration by N leads to a proportional scaling of both length scales, $\Delta h_m = \Delta H_p/N$ and $l_m = l_p/N$, hence $i_m = i_p$.
- **Alternative B**: Assume that $i = \Delta H/(l\rho g)$ is driven by a dimensionless pressure difference ΔH between two points separated by a distance l. Therefore, increasing the model acceleration by N leads to the similitude between model and prototype pressures as $\Delta H_m \equiv \Delta H_p$ while the distance scales by $l_m = l_p/N$ and $a_m = Ng$, leading to $i_m = i_p$.

For both alternatives, and similarly as in the scaling of diffusive processes, when viscosity is not scaled, the soil permeability is N times larger $k_m = Nk_p$ and Darcy's fluid velocity between model and prototype scales by the soil permeability change as $v_m = Nv_p$. Hence, the time necessary for travelling a distance l is $t_m^{\text{kin}} = t_p^{\text{kin}}/N^2$, matching the diffusive time scale. If the fluid viscosity is scaled in the model, such that $\mu_m = N\mu_p$, but its density is kept constant $\rho_m = \rho_p$, the soil model permeability and flow velocity in the model would match that in the prototype, such that $k_m = k_p$ and $v_m = v_p$, respectively. Therefore, the time for travelling the distance l is now $t_m^{\text{kin}} = t_p^{\text{kin}}/N$, matching again the diffusive time when the fluid viscosity is scaled.

Finally, if the grains inertia increases, it is expected for viscous forces to become less dominant and the flow regime to transition to a more agitated system. Grain-to-grain interactions in a centrifuge model are described in Cabrera et al. (2020) as a combination of frictional contacts, proportional to F_D as $N^{1/2}$, and inertial interactions, proportional to $N^{1/6}$. The addition of these provide an estimate to the model velocity increasing by $N^{2/3}$. Adding the role of a scaled viscous fluid, $\mu_m = N\mu_p$ shows that transitional flow regimes can be retrieved and match those observed in the field (Cabrera et al.

2018), but the extend to which fluid forces govern the deformation of the granular flow remains unknown. Further work is necessary for improving our understanding of the centrifugal acceleration effect on highly inertial saturated flows.

In summary, scaling fluid flow through porous media requires accounting for the similitude between diffusion, dynamic, and kinetic processes. Achieving this similarity requires identifying the governing processes in the prototype and matching those through a physical modelling strategy. Here, we advocate that for models focused solely on diffusion and kinetic processes, scaling the fluid viscosity is not necessary. However, if dynamic processes are of interest, appropriate scaling of the fluid viscosity becomes imperative (see Table A1).